

Secondary-electron-production cross sections for electron-impact ionization of helium

R. R. Goruganthu and R. A. Bonham

Department of Chemistry, Indiana University, Bloomington, Indiana 47405

(Received 16 December 1985)

Measurements of the double-differential cross sections (DDCS) as a function of the ejected energy, angle, and primary energy for electron-impact ionization of helium are reported at incident energies of 200, 500, 1000, and 2000 eV. The ejection angle is varied from 30° to 150° in steps of 15°. The cross sections were obtained by use of a crossed-beam apparatus with an effusive gas source and a pulsed electron beam. Scattered and ejected electrons were energy analyzed by time-of-flight analysis from 2 eV to the primary energy as a function of the ejection angle. The relative measurements were normalized by matching the experimental elastic differential cross sections to absolute measurements at selected angles. Comparisons of the DDCS with available literature values revealed significant differences. At 2000 eV impact energy, first-Born-approximation calculations of the DDCS were found to be in agreement with the present data for ejected energies between 2 and 40 eV. At large angles and lower incident energies the Born calculation results are lower than the present DDCS. The DDCS were fitted with a Legendre-polynomial expansion as a function of ejection angle for fixed ejected and primary energies. The energy distributions of ejected electrons derived from these fits are presented and used to calculate the total ionization cross section.

I. INTRODUCTION

Ionization cross sections are needed in the modeling of radiation damage of materials and biological matter, in the development of high-power switching devices, energy deposition studies, and in plasma and radiation physics.¹ There are a variety of measured ionization cross sections. While the primary ionization process is very dependent on the nature of the ionizing radiation, the secondary ionizations and dissociative excitations are largely due to the lower-energy ejected electrons produced in the primary process. In this regard the electron-impact ionization cross sections play an important role. The energy and angular distributions of secondary electrons are obtained by measuring the cross section, σ , differential in ejected energy W and solid angle of detection Ω , and as a function of primary energy T , as $d^2\sigma/dW d\Omega$. This will be referred to as the double-differential cross section (DDCS).

There have been extensive studies on the electron-impact ionization of helium. Since helium is the simplest atomic system with more than one electron for which accurate theoretical calculations are possible, it is of special interest for the calibration of experimental techniques. The earliest measurements date back to the 1930s and were reported in two studies, one by Mohr and Nicoll² and a later one by Goodrich.³ Only in the past 20 years have new measurements been reported on these DDCS. Extensive experimental results for the DDCS for He, N₂, and O₂ at impact energies from 50 to 2000 eV in the angular range of 30°–150° were reported by Opal, Beaty, and Peterson.⁴ In their study the ejected energy was investigated from 4 to 200 eV. Oda *et al.*⁵ reported measurements made at a primary energy of 500 eV in the angular range 10°–130°. Their lowest ejected energy was 24 eV. Rudd and DuBois⁶ have measured the absolute DDCS at primary energies of 100 and 200 eV in the angu-

lar range 10°–130° using a static gas cell. Their DDCS for low ejected energy exhibited a peak in their angular distribution below 30°. Shyn and Sharp⁷ have reported the DDCS using a beam-beam experiment for impact energies of 50, 100, 200, and 300 eV in the angular range 6°–156°. These authors have also noticed the above-mentioned forward peak. Very recently Erhardt *et al.*⁸ have measured the DDCS in the angular range of 18°–150° for ejection energies of 2, 4, 10, 20, and 40 eV. Their primary energies ranged from 100 to 600 eV. These authors have used the same apparatus as the one with which they made ($e, 2e$) measurements. These measurements do not show forward peaking.

Theoretical calculations of these quantities are surprisingly few. Bell and Kingston⁹ have calculated the DDCS in the Born approximation using a truncated partial-wave expansion of a Coulomb wave for the ejected electron. These authors used an explicitly correlated wave function for the He ground state. Less sophisticated calculations employing the impulse approximation have been reported.¹⁰ Significant advances in the data analysis to bring out the systematics in these quantities have been reported by Kim.¹¹ Recently Kim has published recommended DDCS based on the then available experimental data.¹²

In this paper we present experimental measurements of the DDCS for ionization of helium by 200–2000-eV electrons in the angular range 30°–150° using a crossed-beam apparatus. This is the first experimental measurement of the DDCS using time-of-flight (TOF) velocity analysis of the ejected electrons. All the previous experimental determinations used electrostatic electron energy analyzers. The present data were normalized by matching the elastic scattering intensity to absolute measurements and theory. Comparisons of our data with the available literature data are presented. The energy and angular distributions are of higher estimated accuracy than most previously published results.

II. EXPERIMENTAL

A schematic diagram of the apparatus used in the present experiment is shown in Fig. 1. The apparatus consisted of a pulsed electron-beam source, an effusive gas source, and a rotatable detector to change the scattering angle. We have used commercially available electron guns¹³ for producing the electron (e) beam. In most of the experiments tungsten filaments were used. The gun had an Einzel lens for focusing and two orthogonal pairs of deflector plates. dc electron-beam currents of 0.5 to 2.0 μA were obtained for beam energies of 400 to 2000 eV. The deflector plates were used to direct the beam through the scattering center and on to a prepositioned beam trap. We employed a zoom lens to decelerate, when necessary, the beam energy to half its original value. In this way we were able to get high beam currents with the gun 45 cm from the scattering center. This lens was also used to refocus the electron beam. As shown in Fig. 1, the beam passed through two skimmers with apertures of 1 mm diameter. There were an additional pair of deflector plates between the two skimmers for double pulsing the electron beam and to guide the e beam through the second skimmer. These experiments did not use the double-pulsing provision. After applying the required potentials on the plates to align the electron beam, the beam was pushed aside by biasing a deflector plate. To the other plate, a negative going pulse of 10 to 15 V with a rise time of 1 ns and a pulse width of 40 ns was applied. The pulse was delayed and applied to one of the other pair of deflector plates. This procedure made the beam trace a rectangle. The aperture was centered on one of the sides of this rectangle. An electrically isolated ring, with applied positive

voltage, was placed around the conical skimmer to prevent any secondary electrons from entering the scattering region. The other unused skimmer was also biased in the same fashion for the same purpose. The measured dc electron-beam diameter [full width at half maximum (FWHM)] was found to be less than 1 mm and had a calculated maximum divergence of 0.25° neglecting space-charge effects. This divergence accounted for a 0.4-mm beam width at the scattering center.

The collision chamber was 17.5 cm in diameter and 30 cm high. Two ports, diametrically opposite, on the collision chamber were used to admit the e beam, and to mount a flight tube provided with a movable Faraday trap and collimating apertures to probe scattered electrons at small angles. (This port will be referred to as the primary arm.) The electron-beam direction makes an angle β of 20.2° with respect to the horizontal plane. Equivalently, the e -beam direction makes an angle of 69.8° with the collision chamber axis. At the end of the primary arm a detector, consisting of two microchannel plates (MCP), was placed and could be moved by $\pm 3^\circ$ on either side of the Faraday trap. This detector however, was not used in this experiment.

The gas inlet tube was 0.5 cm in inner diameter and was attached from the chamber lid. The tube axis was perpendicular to the e -beam direction and was provided with x , y , and z motions. The end of this tube was terminated in a platinum hypodermic needle of 0.280 mm inner diameter and of 0.5 cm length. The aspect ratio of this nozzle was found to give a tenfold increase in the gas density in the scattering region over the background pressure. An additional gas inlet tube of 0.5 cm inner diameter was placed 6 cm away from the scattering center. Tar-

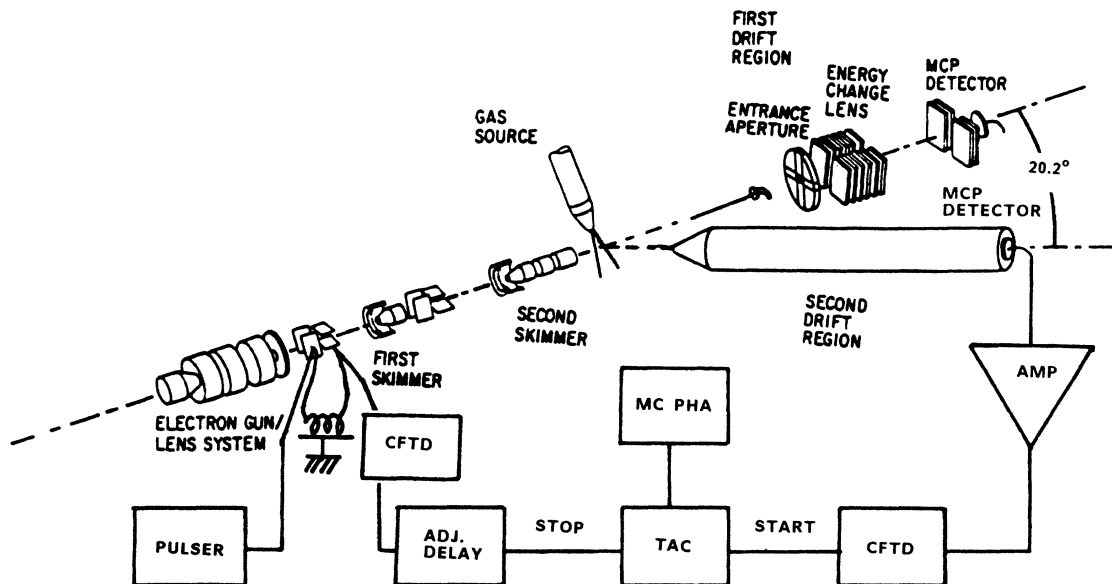


FIG. 1. Schematic view of the pulsed electron-beam time-of-flight apparatus. The second drift tube moves in a horizontal plane about the scattering center and the electron-beam direction is 69.8° with respect to its rotation axis. CFTD stands for constant fraction timing discriminator. STOP and START are the stop and start inputs to the TAC. MC PHA is a multichannel pulse height analyzer and AMP stands for amplifier.

get gas could be admitted into this tube for background scattering measurements.

On one side of the collision chamber a 2-cm-wide slot was cut halfway around it to probe secondary electrons in the horizontal plane. The slot was covered by a concentric cylinder and this cylinder could be rotated by a gear mechanism. There were two *O*-ring seals between the rotatable and chamber cylinders, one above and one below the slot. The rotatable cylinder carried a tube of 3.8 cm inner diameter and 22.9 cm in length for electrons to drift through. An electron detector consisting of two MCP's arranged in a chevron configuration was placed at the end of the drift tube. A 95% transparent graphite-coated copper grid was positioned 6 mm in front of the detector. Electrons entering the flight tube were accelerated by 253 V between this grid and the MCP front surface. There was a single defining aperture in a cone at the entrance end of the drift tube. This aperture was 2 mm in diameter and was 8 cm from the scattering center. The active area of the detector was 18 mm in diameter and was 43.8 cm away from the scattering center. The solid angle subtended by this detector was calculated to be 3.8 msr and its angular resolution was about 2°.

A gear fixed to the rotating cylinder was mechanically driven. A mechanical counter recorded the angle α between the secondary arm and the projection of the *e*-beam direction in the horizontal plane whenever the gear was rotated. The scattering angle θ is given by

$$\theta = \cos^{-1}(\cos\alpha \cos\beta), \quad (1)$$

where β is 20.2° as defined earlier. A ten-turn potentiometer (100 k Ω) was coupled to the gear on the rotating cylinder, giving another check on the angular measurement. Ten volts were applied across the potentiometer and the potential at the sliding terminal was measured with an analog-to-digital converter. The secondary arm position was set to 90° and calibrated. The relative angular displacements of the arm from this position were determined from the potentiometer measurement and the counter reading. The potentiometer was calibrated on a divider head. The concordance between the resistance measurement and the mechanical counter reading was better than 0.1°. This system gave the scattering angle to an estimated accuracy of better than 0.3°.

The main chamber was evacuated by an oil-diffusion pump of 15 cm diameter. The diffusion pump was separated from the chamber by a Freon-cooled baffle to minimize the oil vapor reaching the chamber. The effective pump speed of the assembly was 500 l/s. A Welch mechanical pump (speed 50 l/s) was used to back the diffusion pump. A 5 cm oil-diffusion pump assembly was used to differentially pump the gun region and had an effective speed of 25 l/s. The ultimate pressures obtained were 4 μ Torr in the chamber region and 1 μ Torr in the gun region.

The whole apparatus was constructed of aluminum and brass except for the pumping systems. All parts of the apparatus in the electron path were made of aluminum and were coated with colloidal graphite (Aerodag) to minimize the production of secondary electrons arising from the collisions of electrons with the metal surfaces, and to

make a conducting equipotential surface.

The apparatus was surrounded by a pair of tilted Helmholtz coils to compensate for the Earth's magnetic field. The whole apparatus was enclosed in a wooden box lined with a highly permeable magnetic shield made of μ -metal sheet of thickness 0.45 mm. The magnetic field inside the shield was less than 2 mG and was uniform within 1 mG. The drift tube was covered with an additional μ -metal shield to further reduce the magnetic field along it. All shields were degaussed before each measurement by passing a variable alternating current through coils surrounding them.

Ultrahigh-purity grade helium (99.999%) obtained from Matheson Inc. was used in these experiments. Helium gas was admitted to the nozzle through an adjustable leak valve such that the background pressure in the chamber rose from 4 to 160 μ Torr. The flow rate of helium through the nozzle was calculated to be 2.5×10^{18} atoms/s. We have measured the gas beam profile by monitoring the scattered electron intensity at 90° scattering angle as the nozzle was scanned in a direction perpendicular to the *e* beam. From this a FWHM of the gas beam was found to be 1 mm. The size of the interaction region was measured by moving the nozzle along the *e*-beam direction. It was found to be 7 mm in agreement with that calculated by geometric considerations. This assured us that there should not be any angular-dependent path-length correction as long as the background scattering was subtracted from the original scattering intensity.

A block diagram of the electronics used is also given in Fig. 1. The anode pulse from the MCP detector was amplified (Ortec 574 or Phillips Scientific 6954) and discriminated (Ortec 934 or Tennelec 454) and was used to start the time to amplitude converter (TAC) (Canberra 1443A). The pulse applied to the deflector plates was delayed and used to stop the TAC. Again a timing discriminator was used to condition the pulse. The TAC output was applied to a multichannel analyzer (MCA) for pulse height analysis and storage. The MCA stored the event corresponding to a smaller flight time in higher channels and vice versa. The procedure of collecting an inverted time spectrum, in cases where the start pulse rate is much greater than the true conversion rate, was used to decrease the dead time of the acquisition system. The dead time was less than 3% at start pulse rates of less than 1 kHz.

III. DATA COLLECTION

Experiments were carried out at a constant angle after obtaining an electron beam at a chosen primary energy *T*. The TOF spectrum $S(t)$, at a chosen scattering angle θ , was collected for a period of t_1 sec and the gas flow was diverted to the auxiliary nozzle and the background TOF spectrum $S_b(t)$ was recorded for a period of t_2 sec. The spectrum $S_b(t)$ was assumed to be due to scattering by the background gas and nozzle. In all experiments the nozzle scattering was found to be less than 10% of the background scattering. Typically, the nozzle tip was 1.5 mm above the scattering center. The beam current in the skimmer and the Faraday trap were continuously monitored. The spectra S and S_b were scaled to 1 sec acquisi-

tion time and S_b was subtracted from S to obtain I_{sc} , which was related to the DDCCS as

$$I_{sc} = \frac{d^2\sigma}{dW d\Omega}(W, \theta) \frac{dW}{dt} \Delta t \Delta \Omega n_0 I_0 l \eta(W) \epsilon(W), \quad (2)$$

where dW/dt is the time derivative of the ejected energy W corresponding to a flight time t , Δt is the time channel width of the MCA, $\Delta \Omega$ is the solid angle of detection, n_0 is the target gas number density, I_0 is the incident electron current (in units of electrons per second), l is the path length of the e beam through the target gas viewed by the detector, $\eta(W)$ is the detector efficiency for electrons of energy W , and $\epsilon(W)$ is the attenuation factor to account for the decrease in the detected scattered current due to scattering by the rest gas.

In Fig. 2 a typical TOF spectrum is shown. Note the peak before the elastic line due to photons resulting from fluorescent decay of excited helium atoms or ions. An analysis of the photon yield in this experiment at 500 eV impact energy is presented in Appendix A. The zero time channel is to the right of this peak. The distance between the scattering center and the grid before the detector was measured to be 43.8 mm. The flight time of electrons of a given energy to travel this distance and an additional distance of 6 mm from grid to detector in a constant accelerating electric field was calculated using relativistic formulas. The flight time for the elastically scattered electrons was equated to the calculated value for the known energy of the elastic line to establish the time scale. The calculated time for the photons to arrive at the detector (1.5 ns) was compared to that determined by the time scale as a check. There was always good agreement between these two values. The MCA channel width was set to 1.6 ns/channel and the channel width was calibrated using an Ortec 462 time calibrator.

The flight times were converted to energies and the counts were converted to relative DDCCS by dividing them

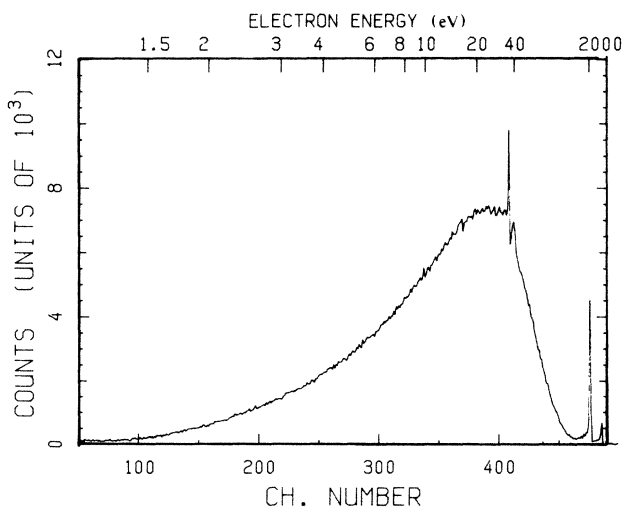


FIG. 2. A typical time-of-flight spectrum. This one was obtained using 2000-eV electrons on He at a scattering angle of 120° . The lower horizontal scale is given in channel numbers which are linearly related to time of flight and the upper horizontal scale shows the scattered electron energy in eV.

by dW/dt . (Since the energy goes as t^{-2} the TOF spectrum has to be multiplied by t^3 to get the DDCCS.) The relative DDCCS as a function of ejected or scattered energy were determined from TOF spectra measured at each scattering angle. The spectra at different scattering angles were corrected for variations in the target density and e -beam current. For each angle θ , a fractional differential scattering cross section (FDCCS) as a function of the scattering angle was defined as

$$\begin{aligned} \sigma_{\text{FDCCS}} &= \int_{10 \text{ eV}}^T dW \frac{d^2\sigma}{dW d\Omega}(W, \theta) \\ &= \frac{d\sigma_{\text{tot}}}{d\Omega} - \int_0^{10 \text{ eV}} dW \frac{d^2\sigma}{dW d\Omega}(W, \theta), \end{aligned} \quad (3)$$

where T is the primary electron energy and $d\sigma_{\text{tot}}/d\Omega$ is the total (elastic plus inelastic) differential cross section. This was measured directly using a single-channel analyzer instead of the MCA at an angle of 90° , then at the angle under consideration, and finally at 90° again. These three measurements took 10 min each to obtain better than 2% statistical accuracy. The procedure was repeated at each angle and the measurement sets for which the two 90° results agreed within 5% were retained for use. All the 90° spectra were then forced to match to obtain the FDCCS angular distribution. The FDCCS values derived from the long-duration individual experiments carried out at different angles were then matched to this FDCCS distribution. This was essentially the same procedure we used in an earlier note.¹⁴ The error in establishing the relative scale by this procedure is estimated to be 6%.

The elastic differential cross section (DCS) at each angle was determined from the relative spectra. In determining the elastic intensity the counts in the five channels centered about the peak were added. The inelastic scattering contributing to this peak intensity was subtracted as described in Appendix B. The elastic DCS at selected angles was matched to the experimental absolute elastic DCS by minimizing

$$\Delta_{\text{err}} = \sum [1 - \alpha Y_2(\theta_i)/Y_1(\theta_i)]^2, \quad (4)$$

where $Y_1(\theta_i)$ and $Y_2(\theta_i)$ are the absolute and relative elastic DCS and α is the scale factor. The uncertainty in α due to the errors in the absolute elastic DCS will be referred to as normalization error and is given in Table I. In this way all the points were weighted equally irrespective of their magnitude.

The relative efficiency as a function of electron energy of the detector used in the present experiments has been previously reported.¹⁵ The detector efficiency at each primary energy was normalized to unity. The DDCCS for a given ejected energy W was divided by the normalized efficiency for that energy.

Finally, a correction for the electron transmission through the rest gas using Beer's law as

$$\epsilon(W) = e^{-nl\sigma(W)} \quad (5)$$

was made, where n is the number density of the background gas, l is the path length, and $\sigma(W)$ is the total cross section (TCS) of He for electrons of energy W . The

TABLE I. Percentage error estimates for the DDCS.

Electron energy	$\gamma(dt/dW)$	$\gamma(\epsilon(W))$	Magnetic field effect	Overall ^{a,b} percentage error
2	1.6	4.1	2.8	-10, +13
4	1.7	3.7	2.0	-10, +12
6	1.8	3.4	1.6	-10, +12
8	1.8	3.1	1.4	-10, +12
10	1.8	2.9	1.3	-10, +11
16	2.0	2.3	1.0	-10, +11
20	2.1	2.1	0.9	-10, +11
40	2.5	1.3	0.6	-10, +10
50	2.8	1.1	0.6	-10, +10

^aThe other energy independent errors are $\gamma(\Delta t)$, 0.5%; $\gamma(\eta(W))$, 2%; relative scale error, 6%; normalization error, 6%; count rate error, 3%.

^bAll the errors are added quadratically except the magnetic field effect which decreases the DDCS. This error was included asymmetrically.

average product of l and the gas density was found to be $2.2 \times 10^{18} \text{ m}^{-2}$. The TCS needed for 2–50-eV electrons were taken from the published results of Kennerly and Bonham¹⁶ and for higher electron energies we employed the data reported by Blaauw.¹⁷ However, for 1- and 2-keV electrons, the TCS were determined by extrapolating the curve fitted to the Bethe-Born formula using the data of Ref. 17.

IV. ERROR ANALYSIS

Errors involved in a scattering experiment to measure angular and energy distributions of scattered electrons can be broken up into those affecting the angular distribution and those affecting the energy distributions. Errors such as the path-length correction¹⁸ arising from the variation of the intersection region of the detector view cone, and variations of the gas and electron beams with the scattering angle, would contribute to the former class of error. Variation of the detector efficiency with energy, the attenuation of the scattered electron signal by the rest gas, background counts arising from known or unknown effects in the spectrometer, the background subtraction procedure, and the spectrometer transmission function for electrons of different energy contribute to the latter class. These sources of error are common to experiments employing electrostatic energy analyzers and the time-of-flight method. A detailed error analysis for a TOF spectrometer used to measure total cross sections for electron-molecule scattering has been given by Kennerly and Bonham,¹⁶ Jones and Bonham,¹⁹ and Jones.²⁰ The current TOF spectrometer is similar to the latter with the added provision for angular resolution of scattered and ejected electrons.

The desired DDCS is obtained from the background-corrected count rate I_{sc} in a TOF spectrum which is proportional to $d^2\sigma/dt d\Omega$. Equation (2) can be rewritten in the form

$$\frac{d^2\sigma}{dW d\Omega}(W, \theta) = \frac{I_{sc}}{\Delta t \Delta \Omega} \frac{1}{n_0 t_0 l \eta(W) \epsilon(W) (dW/dt)}, \quad (6)$$

where all the parameters have the same meaning as before. From this equation some readily identifiable errors can be listed as follows.

1. Statistical accuracy in the measured counts: The standard deviation in the measured number of counts is given by the square root of the number of counts. In the present experiment a normalized (to 1 sec) spectrum obtained after diverting the gas into a remotely located nozzle was subtracted from the one obtained when the gas was flowing through the nozzle into the scattering center. The subtracted count rate I_{sc} was typically about 90% of the unsubtracted count rate. For convenience we can write the standard deviation in the counts as $1.1(I_{sc} t_1)^{1/2}$ where t_1 is the acquisition time.

2. Channel width variation: The TAC-MCA system was analyzed for channel width variation using the method given by Coleman *et al.*²¹ There was no variation in the channel widths within the measurement accuracy of $\pm 1\%$. Repeated channel width calibration employing a time calibrator (Ortec 462) gave an average channel width of $\pm 0.5\%$ estimated accuracy.

3. Error in dt/dW : This error arises mainly due to the error in the flight time t . The relative error in this quantity, $\gamma(dt/dW)$, is given by

$$\gamma(dt/dW) = [(3 \delta t / t)^2 + (2 \delta l / l)^2]^{1/2}, \quad (7)$$

where l is the flight length while δl and δt are the errors in the flight distance and time, respectively. The flight distance uncertainty is less than 1 mm. The uncertainty in the flight time is due to the nonlinearities in the channel widths as well as the uncertainty in the absolute time mark (in Ref. 19 this is referred to as an energy benchmark) for the TOF spectrum. This is established from the position of the center of the elastic line which has a known primary energy. A check on the time scale is possible from the location of the photon line. This check was always made in all the spectra. An error in the absolute time mark was estimated to be 0.8 ns or half a channel width. Using these numbers a formula for $\gamma(dt/dW)$ in the form of $[a + b(\Delta t/t)^2]^{1/2}\%$ with $a=2.5$ and $b=22\,500$ was obtained.

4. Error in the relative detector efficiency: The relative detector efficiency is determined experimentally to within $\pm 2\%$. The details of this determination and the analytic expression for η have been given by Goruganthu and Wilson.¹⁵ The same detector was used in the current experiments. The amplifier and the constant fraction timing discriminator (CFTD) were changed in an effort to increase the signal in some of the experiments. The TOF spectrum taken with the new amplifier and CFTD was compared with that obtained using the old set of electronics. There was no change in the shape of these two spectra. The comparison experiment was repeated at different angles to establish that the shape of the relative detector efficiency as a function of electron energy does not depend on the post-signal-processing electronics or the ejection angle.

5. Error in the absorption correction: The absorption

correction is about 14% for 2-eV and 3% for 50-eV electrons when the rest gas pressure is 160 μ Torr. Taking an estimated accuracy in the pressure measurement of $\pm 30\%$, allowing for absolute temperature variations of 3%, and a $\pm 3\%$ error in the total cross sections, the relative error in ϵ , $\gamma(\epsilon)$, is given by

$$\gamma(\epsilon) = 0.303 \ln \epsilon. \quad (8)$$

6. Error in establishing the relative scale: The procedure of establishing the relative scale was detailed in Sec. III. The error in the relative scale is obtained from reproducibility of the measurement and is generally better than $\pm 6\%$. In establishing this scale the low-energy electron contribution to the total count rate which is sensitive to transmission changes was excluded.

Apart from the above obvious errors, special attention to the background counts originating from wall scattering and or aperture scattering is warranted. In a TOF spectrum random start pulses (start pulses unrelated in time with the stop pulse) have a constant probability for conversion and produce the same background in every channel. Typical sources of these pulses include the noise pulses from the MCP's and any pulses produced from metastable helium atoms which have flight times several multiples of the experimental duration of 2 μ s. This background is taken as the count rate in the channels preceding the occurrence of the photon line. This method was employed in Refs. 16, 19, and 20. A significant number of uv photons were detected and nearly all of these were distributed in channels preceding the elastic line with a peak occurring at a flight time of 1.5 ns. The photon contribution to the elastic line was negligible.

A second source of potential error is secondary electrons produced at the aperture by electrons and photons. This is also a problem in experiments employing electrostatic analyzers. The aperture scattering is due mainly to elastically scattered electrons hitting the aperture (whose diameter is 2 mm) which can produce secondary electrons that travel down the flight tube to the detector. To minimize this effect, the aperture was made in a cone of semivertical angle of about 30° and coated with colloidal graphite to reduce secondary emission. Assuming the aperture to be of a finite thickness of 0.25 mm the solid angle subtended by the walls of this aperture at the scattering center is calculated from the formula,²²

$$\Delta\Omega = 2\pi \left[\frac{a}{(r^2 + a^2)^{1/2}} - \frac{b}{(r^2 + b^2)^{1/2}} \right], \quad (9)$$

where r is the radius of the aperture and a and b are the distances from the scattering center to the front and rear surfaces of the aperture, respectively. In our experimental configuration, this turns out to be 2.5 μ sr while the aperture solid angle is 420 μ sr. This suggests that the maximum aperture scattering is 0.6% of the detected signal. The ratio of photons to the elastically scattered electrons is typically less than 0.1. Hence, the detected photon-produced secondary electrons are negligible ($< 0.06\%$). The maximum secondary emission yield for carbon²³ is about 1 and occurs at a primary energy of about 300 V. The angular distribution of these secondaries from poly-

crystalline surfaces^{23,24} such as colloidal graphite is known to be a cosine distribution about the normal to the surface. Since the electrons hit the aperture walls at a grazing angle of about 0.6° , the effective probability for these secondaries to hit the detector is calculated to be 2.4×10^{-5} and this translates to less than a 0.3% effect on the number of counts in any channel. It is to be noted that there are *no* other apertures between the scattering center and the detector. No detailed analysis on the possibility that secondary electrons produced in the flight tube will contribute to the signal was made. However, it cannot be a significant effect because the value of the cosine distribution at the near-zero glancing angles accepted by the detector is very small.

Electric and magnetic fields could affect the angular distributions of the scattered electrons. These would also affect the transmission of the electrons through the flight tube depending on the energy of the electron. Precautions were taken to minimize punch through fields from the zoom lens and no known electrostatic fields were present between the scattering center and the detector. Magnetic field compensation was discussed in Sec. II. No ac magnetic fields were measurable. The magnetic field effect on a 1-eV electron was calculated to be negligible. In this calculation it was assumed that the electrons originated from a point. Since the solid angle is limited by the aperture and not by the detector, there would not be any loss in the detected signal due to the bending of the electron trajectories by the magnetic fields. However, since the scattering occurs from points distributed approximately in a Gaussian shape about the scattering center with a FWHM of 1.5 mm, a rough calculation suggests a maximum possible error of 4%. Since the magnetic field is not measured over the whole region, this estimated correction was not made. Further, the maximum angular error in the scattering angle because of the magnetic field was estimated to be less than 0.1° . This effect on the DDCS should be negligible for low-energy electrons, since the DDCS varies very slowly with angle. The magnetic field effect on fast scattered electrons, for which the DDCS is strongly angle dependent, is smaller.

The influence of patch effects on the measured cross sections is very complicated to model. It was reduced by designing the flight tube to have a diameter several times the entrance aperture on the cone.^{19,20,25} From time to time, when a loss of transmission was detected, the aperture cone and the flight tube were cleaned and recoated with "Aerodag." We were able to regain the previous transmission characteristics. To understand the effect of contact potentials, we studied the low-energy electrons (0.8–2.4 eV) produced in the electron scattering from molecular nitrogen. The positions of autoionizing peaks corresponded to the literature values indicating that the effect on the energy scale is insignificant. However, large transmission effects ($\sim 50\%$) below about $W=4$ eV were occasionally observed. Our observations suggest that the present cross-section values for low-energy electrons will be a lower bound to the true value since any loss in transmission will reduce the cross section.

One further possible source of error affecting the angular distribution is an angular-dependent absorption correc-

TABLE II. Comparison of the DCS for elastic scattering of 200-eV electrons by helium. All results are in units of $10^{-4}a_0^2/\text{sr}$. The scattering angle is denoted by θ . Numbers in square brackets are interpolated values. The number in parentheses is the power of ten by which the preceding number is multiplied.

θ (deg)	Present results	Bromberg ^a	S ^b	Jansen <i>et al.</i> ^c	Crooks and Rudd ^d	Byron and Joachain ^e
30	2.74(3)	2.76(3)	2.63(3)	2.81(3)	3.25(3)	2.91(3)
45	1.15(3)	[1.16(3)]		1.14(3)		
60	5.50(2)	5.57(2)	5.38(2)		[6.60(2)]	5.43(2)
75	279	[313]				
90	191	190	177		233	184
105	138	[131]	[127]			
120	97.1		98		[122]	95.1
135	82.8		[74]			
150	72.1		60		84.3	66.5

^aThese values were cited by Byron and Joachain, Ref. 29.

^bReference 30.

^cReference 26.

^dReference 28.

^eReference 29.

tion due to the fact that the gas inlet is tilted with respect to the ejected electron detection plane. Calculations showed that the correction due to this asymmetry was less than 0.2%.

The effect of all the above cited errors on the DDCS are given in Table I.

V. RESULTS AND DISCUSSION

This section has been subdivided into four parts to present the DDCS and the angular variation of the elastic intensity for each primary energy. Comparisons of the

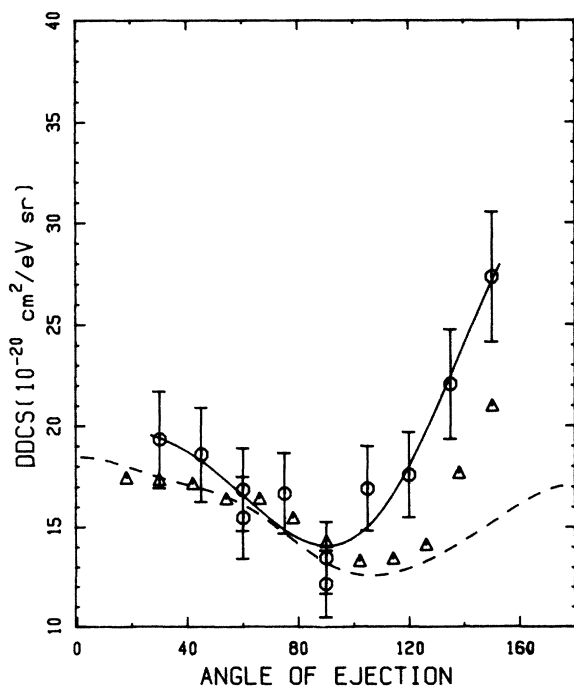


FIG. 3. Absolute DDCS for He for 2-eV ejected energy and a primary energy of 200 eV. Circles denote the present results and triangles those by Erhardt *et al.* Dashed curve is from the recommended values by Kim and the solid line is a fit to an expansion in Legendre polynomials using the present data.

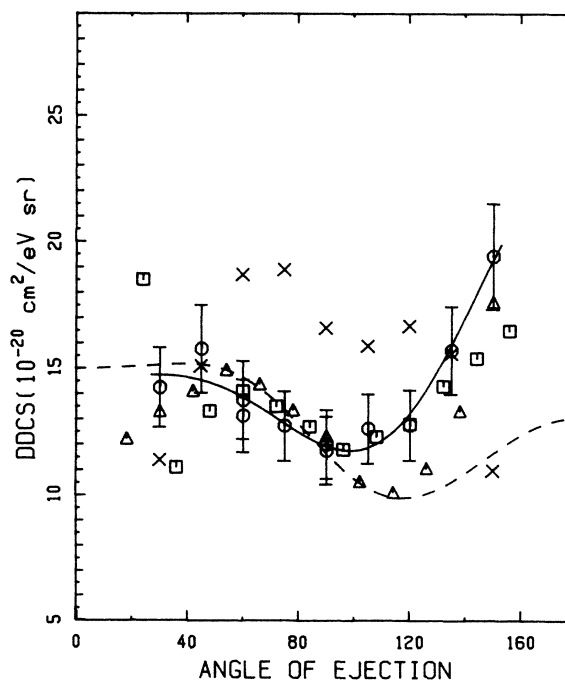


FIG. 4. Absolute DDCS for He for 4-eV ejected energy and 200 eV primary energy. The squares represent the results of Shyn and Sharp and crosses denote those by Opal *et al.* For the definition of other symbols see the caption to Fig. 3.

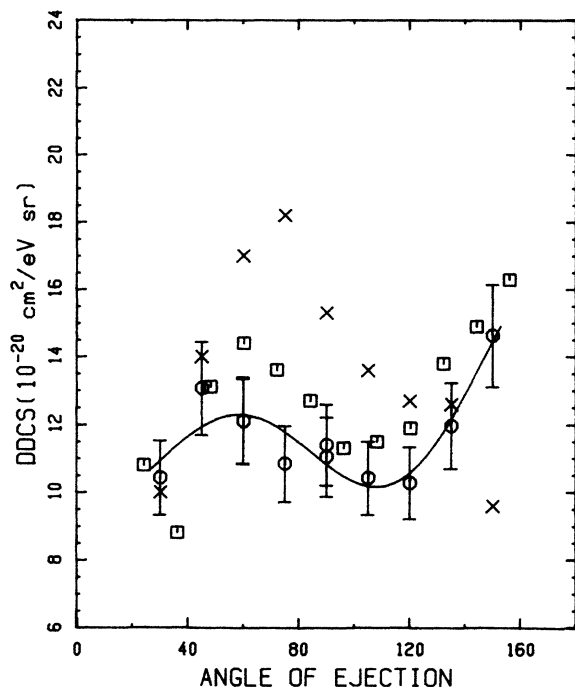


FIG. 5. Absolute DDCS for He for 6 eV ejected energy and 200 eV primary energy. For the definition of symbols see the captions to Figs. 3 and 4.

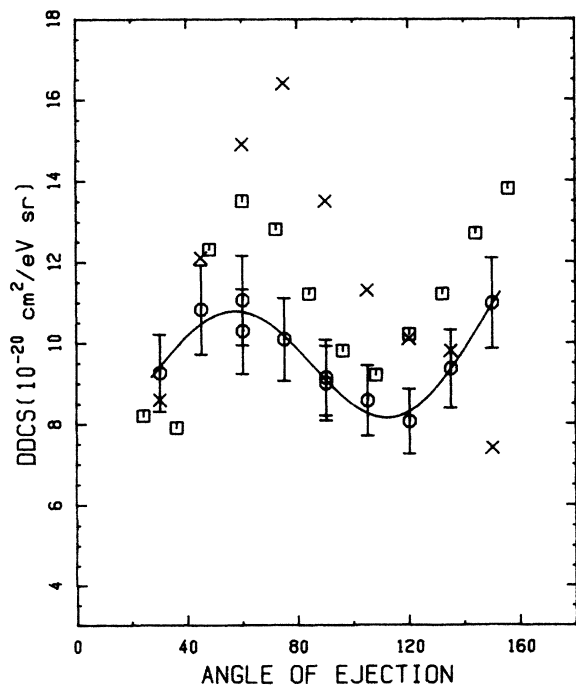


FIG. 6. Absolute DDCS for He for 8 eV ejected energy and 200 eV primary energy. For the definition of symbols see the captions to Figs. 3 and 4.

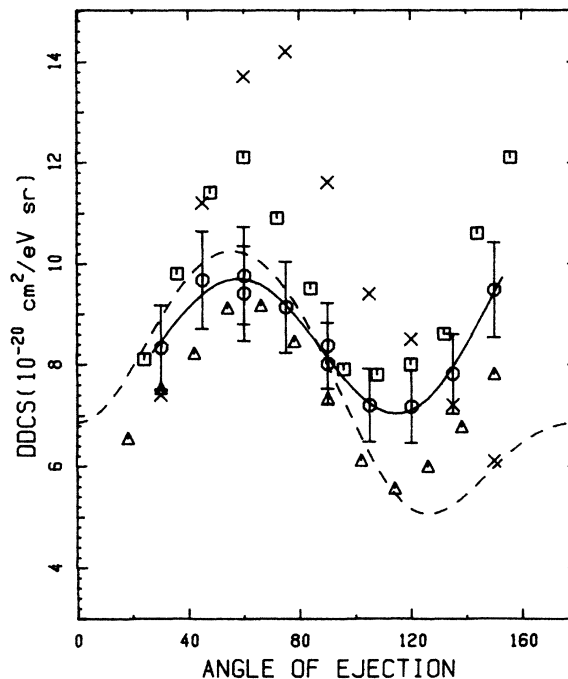


FIG. 7. Absolute DDCS for He for 10 eV ejected energy and 200 eV primary energy. For the definition of symbols see the captions to Figs. 3 and 4.

elastic differential cross sections with the available literature data are presented at each energy in a tabular form.

A. 200-eV primary electrons

The experiment was carried out at scattering angles of 30°, 45°, 60°, 75°, 90°, 105°, 120°, 135°, and 150°. The experiment was repeated at scattering angles of 60° and 90°. Since at this energy the energy resolution in the elastic peak was 25 eV, there is no significant inelastic intensity contribution to the elastic peak (see Appendix B). We selected for normalization the elastic DCS at 45° reported by Jansen *et al.*²⁶ ($\pm 6\%$) and the ones at 60° and 90° by Bromberg²⁷ ($\pm 3\%$). A normalization factor was so chosen (as described in Sec. III) to best scale the present relative elastic DCS data to these selected values. The normalized elastic DCS are presented in Table II. Note that the experimental values at 60° and 90° are the average of two independent measurements.

The experimental elastic DCS is estimated to have an accuracy of $\pm 12\%$. An examination of Table II indicates that the present experiment agrees very well with the theoretical values of Byron and Joachain²⁸ and that the angular shape is in close agreement with that of Crooks and Rudd,²⁹ whose values are about 20% higher than the present results. At large angles the results of Sethuraman *et al.*³⁰ fall off faster than the present experiment. Finally, there is good agreement in shape between the present results and those of Bromberg.²⁷

The photons produced were found to be isotropically distributed at this and the other primary energies. An account of the expected photon yield in the present experiment is given in Appendix A. Although the calculation

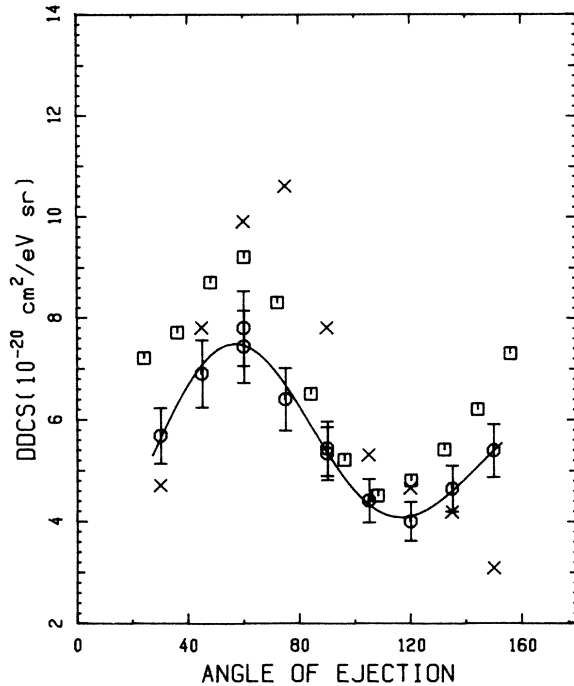


FIG. 8. Absolute DDCS for He for 15.9 eV ejected energy and 200 eV primary energy. For the definition of symbols see the captions to Figs. 3 and 4.

presented there was for 500-eV electrons the conclusions are equally valid for this and the other primary energies. A high degree of radiation trapping is shown to be present in the experiment. The isotropic distribution of photons served as an additional check on the relative scale determination.

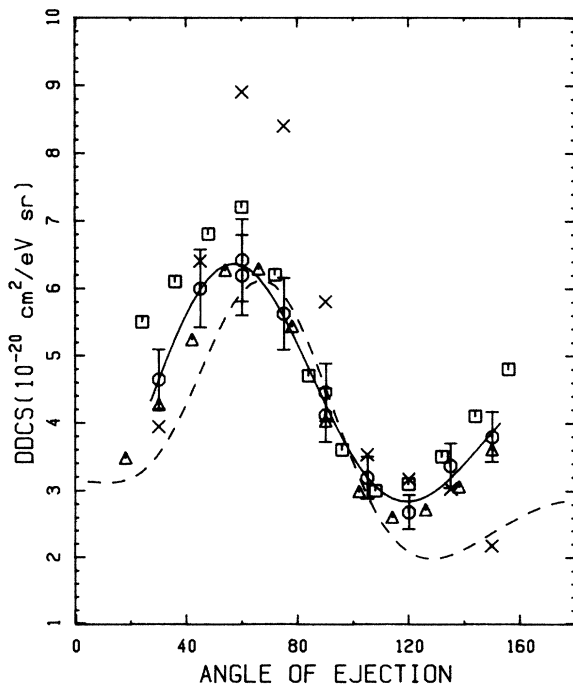


FIG. 9. Absolute DDCS for He for 20 eV ejected energy and 200 eV primary energy. For the definition of symbols see the captions to Figs. 3 and 4.

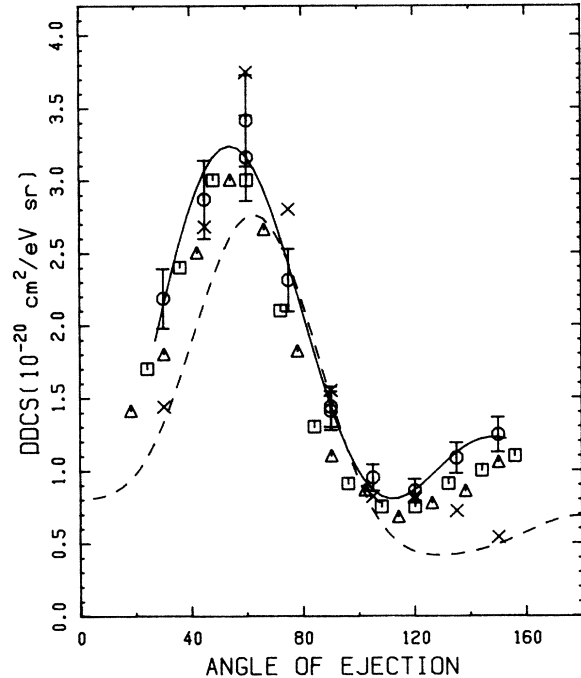


FIG. 10. Absolute DDCS for He for 40 eV ejected energy and 200 eV primary energy. For the definition of symbols see the captions to Figs. 3 and 4.

The DDCS at 2, 4, 6, 8, 10, 15.9, 20, 40, and 50 eV ejection energy were plotted as a function of the ejection angle as shown in Figs. 3–11. The DDCS at these ejected energies were obtained by Lagrange's interpolation formula³¹ since it strongly weights the experimental points in the vicinity of the point being interpolated. By altering the

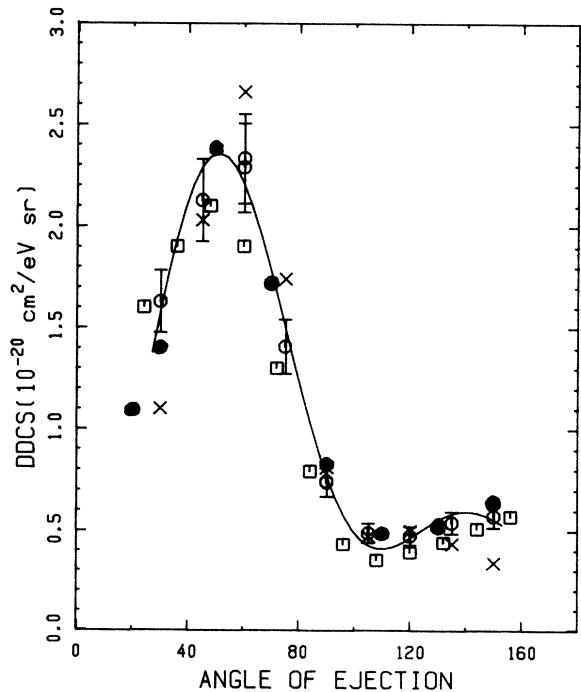


FIG. 11. Absolute DDCS for He for 50 eV ejected energy and 200 eV primary energy. The solid circles denote the measurements by Crooks. For the definition of other symbols see the captions to Figs. 3 and 4.

number of points for interpolation, the error in the interpolation was investigated and found to be within the statistical accuracy. Procedures using window averaging in the neighborhood of the selected ejection energy also gave similar values in most cases. At ejection energies between 35.5 and 39.1 eV the ionization lines arising from the states $2s2p$ and $2s3p$ were observed. The interpolation was done carefully for the ejected energy of 40 eV because of the strong variations of the DDCS with energy around this value.

In Figs. 3–11 the present results were denoted by circles together with the uncertainties in the measurements. Where possible, the measurements by Opal *et al.*⁴ are shown by crosses. These values were cited to have an estimated accuracy of $\pm 25\%$. The results of Shyn and Sharp⁷ are indicated by squares and have an estimated accuracy of $\pm 17\%$. Also shown, by triangles, are the measurements by Erhardt *et al.*⁸ with accuracy of $\pm 15\%$ in absolute magnitude and $\pm 2\%$ in the angular shape. The suggested values of Kim¹² are given by the dashed curve computed from his Legendre-polynomial coefficients. The solid line in these figures is the result from a least-squares fit of the DDCS to an expansion in Legendre polynomials of the form

$$\frac{d^2\sigma}{d\Omega dW} = \sum_{n=0}^4 A_n(W)P_n(\cos\theta), \quad (10)$$

where P_n is the n th-order Legendre polynomial and θ is the ejection angle and the coefficients $A_n(W)$ are functions of the ejected energy W and incident energy T .

The present results for the DDCS are in good agreement with the measurements of Erhardt *et al.*⁸ in angular shape of ejected energies between 2 and 40 eV. At 2 eV ejected energy, both the present results and those of Erhardt *et al.* show a rapid increase in the DDCS with angle in the backward direction. This feature is missing in the suggested DDCS of Kim.¹² This trend continues up to ejection energies of about 20 eV. The peak in the angular distribution in the range of 45° to 90° of ejection angle grows with increasing ejected energy. This feature, due to knock-on collisions, is well understood and has been discussed by several authors.³² The results of Opal *et al.* disagree in shape and magnitude with the present results. Their values seem to disagree most for 30° and 150° of ejection angle. The same observation was made by Shyn and Sharp,⁷ Rudd and DuBois,⁶ and Kim.¹² In Figs. 4–11 the data of Shyn and Sharp for very small ejection angles are not shown. At 4 eV their DDCS at 6° ejection angle is 4 times the upper limit of the ordinate of our plot. To bring out the differences among the different measurements on a sensitive scale, their data below 24° ejection angle were omitted. Their measurements show a dramatic increase in the DDCS below about 36° of ejection angle. This type of behavior is not indicated in the data of Erhardt *et al.*⁸ and is in disagreement with the present results at 30° ejection angle. Shyn³³ employing the same apparatus has reported forward peaking in the DDCS for molecular nitrogen. Interestingly, the same feature was reported by Rudd and DuBois who employed a static gas cell. However, the measurements by Shyn and Sharp were made with a beam-beam apparatus with the

gas pressure around the scattering center only a factor of 3 higher than the background pressure. One might guess that experiments using static gas cells or little gas beam collimation may have something to do with such a feature being present. This forward peak was also absent in the suggested values by Kim,¹² who cited the work of Oda and Nishimura³⁴ concluding that the peak is an experimental artifact. Although explicit comparisons of the present data with that reported by Rudd and DuBois were not presented in Figs. 3–10, an examination of the figures in Ref. 7 suggest that at 20 and 40 eV ejected energy the results of Rudd and DuBois⁶ are in good agreement with those by Shyn and Sharp⁷ but at 10 eV the Rudd and DuBois⁶ results are slightly lower than those by Shyn and Sharp.⁷ Therefore, whatever was said above about Shyn and Sharp's data in light of the present experiment will hold true with the results of Rudd and DuBois. In Fig. 11 a comparison of the present data with those of Crooks,²⁸ who made measurements on the apparatus later employed by Rudd and DuBois,⁶ for $W=50$ eV is presented. The agreement seems to be quite good for this ejected energy.

The DDCS integrated over the ejection angle yields a quantity $d\sigma/dW$ called the single differential cross section (SDCS). From the least-squares fits to the Legendre-polynomial expansion in Eq. (9) the SDCS is obtained from A_0 as

$$\frac{d\sigma}{dW} = 4\pi A_0(W). \quad (11)$$

In the least-squares-fit procedure the number of coefficients was varied from 3 to 7 and the fit to the DDCS was studied in each case. Typically, five coefficients seem to give the most reasonable fit to the experimental data. The variations in the value of A_0 with the number of coefficients were small ($< 3\%$ going from 4 to 6 coefficients) and hence the error in determining the SDCS by this procedure was estimated to be 3%. If the errors in the DDCS were random the error in the fit coefficient A_0 would be smaller than the individual random errors in the data points. This was confirmed by adding 10% uniformly distributed random noise to the values obtained from the fit coefficients of Kim¹² and least-squares fitting of the resulting data. Comparisons of SDCS among different experimental results should depend only on systematic errors such as the absolute scale normalization and variations in the energy distributions caused by variable transmission through the analyzer for different velocity electrons.

Plots of the SDCS as a function of the ejected energy for two targets such as helium and nitrogen look about the same. Hence, there is very little information conveyed by them. Further, the SDCS increases rapidly as the ejected energy approaches zero. If one were to obtain the total ionization cross section from such a plot by a straightforward integration over the ejected energy, it would be necessary to know the data for very low energies very accurately. It was pointed out by Kim¹¹ that a modified SDCS, $Y(E, T)$, plotted as a function of the inverse of the energy transfer in the collision amplifies the structure in the low-energy portion of the SDCS. This was referred

to as the Platzman plot. The variable $Y(E, T)$ is defined as

$$Y(E, T) = \frac{d\sigma}{dW} / \left[\frac{d\sigma_R}{dE} \right] = \frac{d\sigma(T)}{dW} \frac{T}{4\pi a_0^2} \frac{E^2}{R^2}, \quad (12)$$

where T is the primary electron energy, E is the energy transfer in the collision leading to the production of a secondary electron of energy W , a_0 is the Bohr radius (0.529×10^{-8} cm), R is the Rydberg constant (13.6 eV), and $d\sigma_R/dE$ is the Rutherford cross section. In the case of helium, E is related to W by $E = W + 24.6$ eV. Electrons originating from autoionization have also been treated as if they are produced by direct ionization. Discussions on graphical procedures can be found in the work of Kim.¹¹ Note that $Y(E, T)$ is dimensionless. In collisions leading to the production of fast secondary electrons, $Y(E, T)$ approaches the effective number of electrons in the target when T is large. A plot of $Y(E, T)$ for 200 eV primary energy is given in Fig. 12 together with the plots for 500, 1000, and 2000 eV.

It was found that the experimental values for Y as a function of R/E can be approximated by an empirical function of the form

$$Y(E, T) = 2 + \alpha / [\beta^2 + (E/R)^2], \quad (13)$$

where α and β are constants which are determined by a least-squares-fit criterion. In Fig. 12 the analytic fit values are represented by the solid line. The total ionization cross section σ_{ion} was calculated using the relationship

$$\sigma_{\text{ion}}(T) = 4\pi a_0^2 \left[\frac{R}{T} \right] \int_{X_1}^{X_2} Y(E, T) d(R/E), \quad (14)$$

where X_1 and X_2 are $2R/(T + 24.6)$ and $R/24.6$, respectively. These kinematic limits are shown in Fig. 12 by the vertical lines. This integral was evaluated analytically to find σ_{ion} using the parameters α and β . This procedure was applied to the calculated DDCS of Bell and Kingston in the Born approximation for 1000 eV primary energy

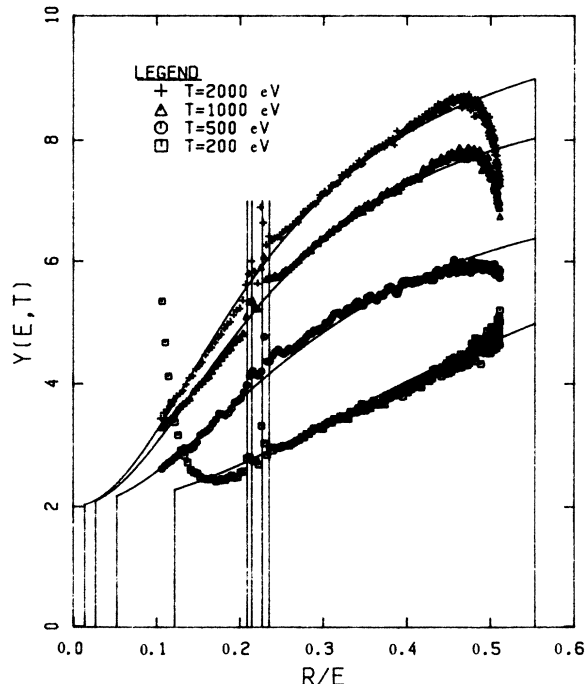


FIG. 12. Platzman plot of the single-differential cross section expressed as $Y(E, T)$ vs R/E where R is the Rydberg unit of energy, E is the energy loss which can be written as the sum of the ionization potential of He and the ejected electron energy, W , and T is the incident electron energy. See Eq. (12) and the associated text for a definition of $Y(E, T)$. The right and left boundaries of Y correspond to ejected electron energies of zero and $(T - 24.6)/2$ eV, respectively. Notice the autoionization lines in the spectrum. The energies for the vertical lines marking the location of autoionizing features were taken from Ref. 50.

and was found to give σ_{ion} to 0.7% accuracy. With the experimental SDCS for $T = 200$ eV, from the above procedure we obtained a value of 0.371×10^{-16} cm² for the total ionization cross section. In Table III comparisons of σ_{ion} obtained by different authors are presented.

TABLE III. Comparison of the reported total ionization cross sections $\sigma_{\text{ion}}(T)$ with the present results for electrons of various incident energies. All numbers are in units of 10^{-16} cm².

Measurement	Incident energy (eV)			
	200	500	1000	2000
This experiment	0.371±0.044	0.221±0.027	0.144±0.017	0.0804±0.0096
Rapp and Englander-Golden ^a	0.347±0.024	0.224±0.016	0.141±0.010	
Smith ^b	0.322 ^c	0.204	0.126	0.0730
Bell and Kingston ^d	0.396 ^c	0.226	0.133	0.0759
Shyn and Sharp ^e	0.290±0.049			
Opal <i>et al.</i> ^f	0.369±0.092	0.242±0.061	0.115±0.029	0.0670±0.017
Rudd and DuBois ^g	0.234±0.059			

^aReference 35.

^bReference 36.

^cNo error estimate is available.

^dK. L. Bell and A. E. Kingston, J. Phys. B 2, 1125 (1969).

^eReference 7.

^fReference 4.

^gReference 6.

TABLE IV. Comparison of the present experimental elastic DCS for 500-eV electrons with literature values. All values are given in units of $10^{-4} a_0^2/\text{sr}$ (i.e., $0.28 \times 10^{-20} \text{ cm}^2/\text{sr}$). See caption of Table II for further details.

θ (deg)	Present expt.	Bromberg Ref. 37	Sethuraman <i>et al.</i> Ref. 30	Oda <i>et al.</i> Ref. 5	Byron and Joachain Ref. 29	Fink and Yates Ref. 38	Jansen <i>et al.</i> Ref. 26
30	945	915	941	922	890	874	933
45	305	288	[276]		257	281	300
60	109	113	111	116	108	115	
75	48.6	[55.5]	[48.3]		53.2	57.1	
90	28.2	31.3	25.4	[31.5]	30.1	33.0	
105	20.1	[20.3]	[15.3]		19.5	21.5	
120	14.9		9.3	[11.5]	13.8	15.4	
135	12.2		[7.5]	[9.3]	10.8	12.1	
150	11.0		6.7		9.04	10.2	

An examination of Table III indicates that the present experiment agrees very well with the measurements by Rapp and Englander-Golden³⁵ and that by Smith.³⁶ However, the results by Rudd and DuBois⁶ are lower than the present results. In general all the other values are in agreement with one another within the error bars.

B. 500-eV primary electrons

At 500 eV primary energy, the experiment was carried out over the angular range of 30° to 150° in steps of 15° . The experiment was repeated at 60° and 90° of scattering. The experiment was also done at 45° and 120° with half the background pressure to study the pressure dependence of the attenuation correction. For this primary energy, we selected for normalization the elastic DCS at 45° reported

by Jansen *et al.*²⁶ and those of 60° and 90° by Bromberg.³⁷ The experimental relative elastic DCS were normalized to these selected elastic DCS by the method outlined in Sec. III. The elastic differential cross sections for 500-eV electrons are presented in Table IV along with the other reported measurements for comparison. Significant corrections for failure to separate elastic and inelastic scattering were applied as outlined in Appendix B.

The angular distribution of the present elastic DCS is in good agreement with the theoretical calculations of Byron and Joachain²⁹ using an *ab initio* optical model theory and the partial-wave calculations of Fink and Yates³⁸ who used a Hartree-Fock-Slater potential. Note that the latter results are higher in the backward direction ($\theta > 90^\circ$) than those by Byron and Joachain. The values of Sethuraman *et al.*³⁰ fall off much faster with angle above 75° than ei-

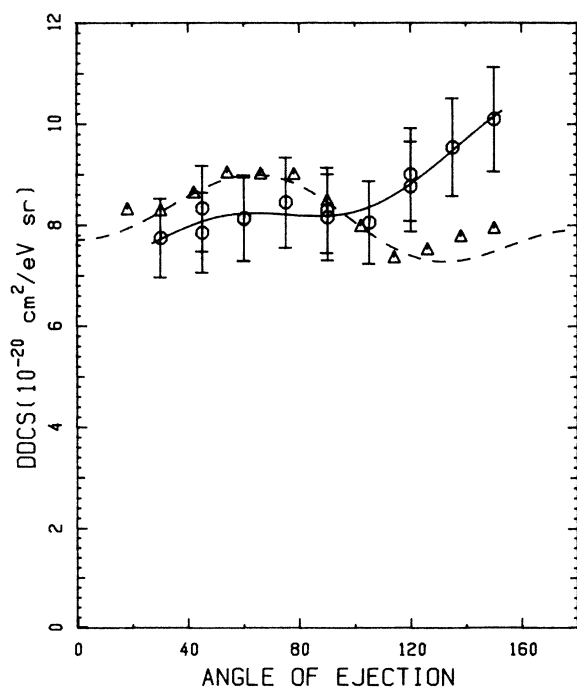


FIG. 13. Absolute DDCS for He for 2 eV ejected energy and 500 eV primary energy. For the definition of symbols see the captions to Figs. 3 and 4.

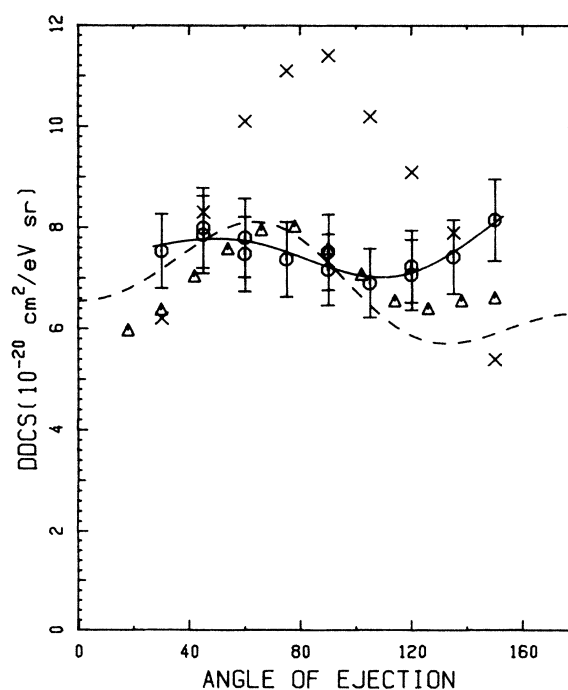


FIG. 14. Absolute DDCS for He for 4 eV ejected energy and 500 eV primary energy. For the definition of symbols see the captions to Figs. 3 and 4.

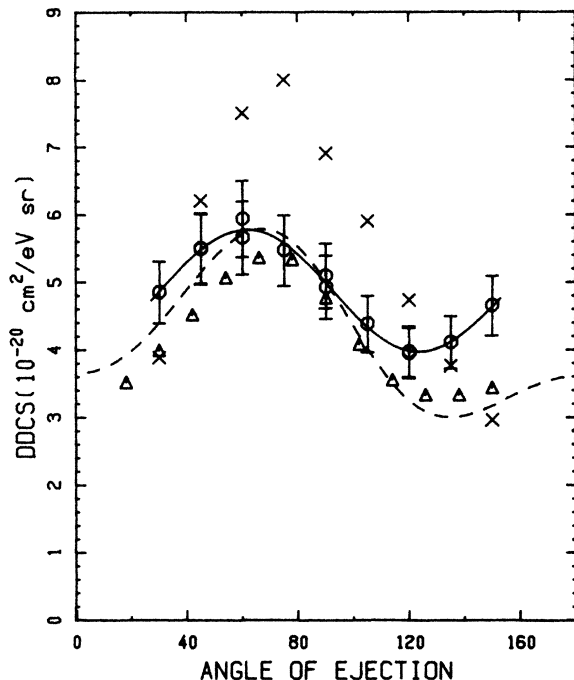


FIG. 15. Absolute DDCS for He for 10 eV ejected energy and 500 eV primary energy. For the definition of symbols see the captions to Figs. 3 and 4.

ther the present results or the two theories.

The DDCS at 2, 4, 10, 20, and 40 eV ejected energy as a function of ejection angle are shown in Figs. 13–17 along with the results by Opal *et al.*, Erhardt *et al.*, and Kim. At 2 eV ejected energy, there is excellent agreement between the results of Erhardt and Kim in shape and magnitude. The present experiments are also in good agree-

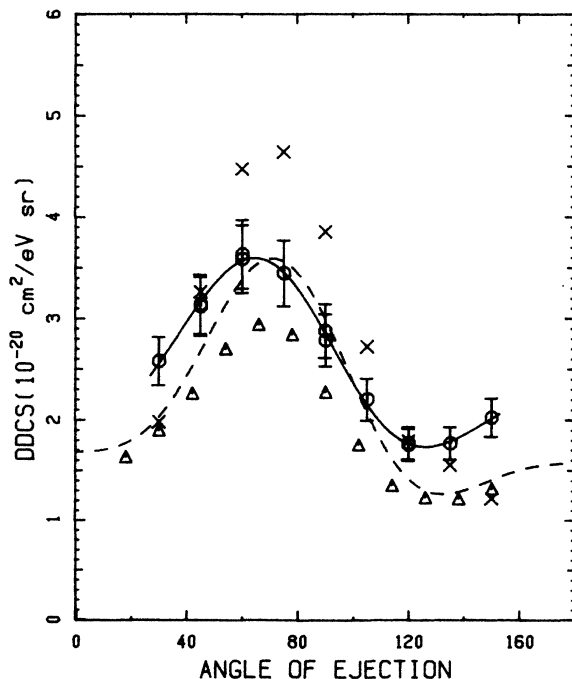


FIG. 16. Absolute DDCS for He for 20 eV ejected energy and 500 eV primary energy. For the definition of symbols see the captions to Figs. 3 and 4.

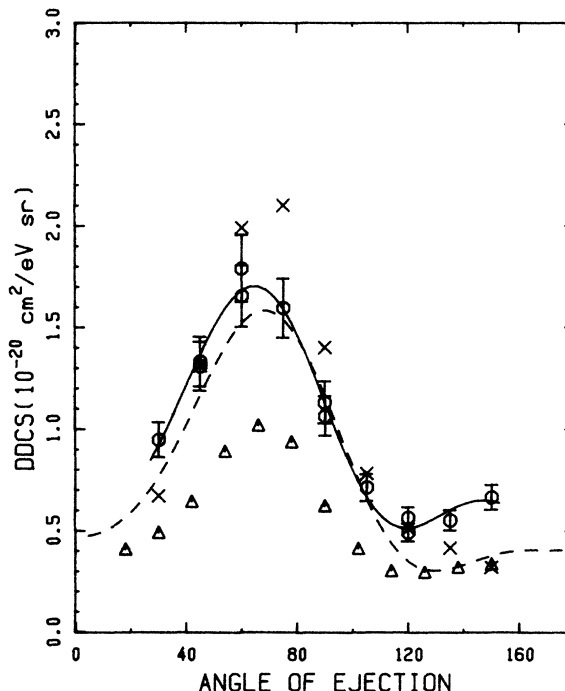


FIG. 17. Absolute DDCS for He for 40 eV ejected energy and 500 eV primary energy. For the definition of symbols see the captions to Figs. 3 and 4.

ment with these two results between 30° and 110°. However, the present results are higher above 110° and seem to hint at the existence of a broad peak in the backward direction. Similar behavior for 2-eV ejected electrons was pointed out in Sec. V A at a primary energy of 200 eV. The present experiments display a trend in the angular distribution with primary energy. The increase in the backward direction at 500 eV primary energy is less pronounced than for 200 eV. At 4 eV the results of Erhardt *et al.* lie slightly above at $\theta > 90^\circ$ and below at $\theta < 90^\circ$ the suggested values of Kim. The present results are still slightly above Erhardt *et al.* and the results by Opal *et al.* are in disagreement with the present results. The situation at 10 eV is essentially the same as that at 4 eV. At 20 eV ejected energy there appears to be good agreement in the shape of the angular distribution between the present results and those by Erhardt *et al.* but the suggested values by Kim are lower at large and small ejection angles than the present experiment. At 40 eV our results are again in agreement with those by Erhardt *et al.* in shape but their results are about 40% smaller in magnitude. Suggested values of Kim are in fair agreement with the present results as are those by Opal *et al.* The disagreement with the data by Erhardt *et al.* is surprising considering the general agreement for 200 eV. The results by Oda and Nishimura³⁴ and Oda³⁹ at 500 eV primary energy were presented at ejection energies of 27.5, 35.5, and 43.5 eV. Their experimental DDCS were normalized at each ejected energy so that the peak heights of the broad maxima in the angular distribution agreed with calculated values employing binary-encounter theory. An examination of their data in the angular range 30° to 130° shows agreement in shape between their results and the present experiment.

The SDCS for 500 eV primary energy shows a monotonic decrease with ejected energy. A plot of $Y(E, T)$ for $T=500$ eV is given in Fig. 12. The total ionization cross section for 500 eV is given in Table III. A comparison with other values suggests agreement among the different results.

C. 1000-eV primary electrons

The experiment was carried out at ejection angles between 30° and 150° in steps of 15° . The experiment was repeated at 60° , 90° , and 120° of scattering. A normalization factor for the relative elastic DCS was found by matching the experimental data at 45° and 90° to the 45° datum by Jansen *et al.*²⁶ ($\pm 6\%$) and to the theoretical elastic DCS by Fink and Yates³⁸ at 90° by the procedure detailed in Sec. III. The present normalized elastic DCS are presented in Table V. The corrections for inelastic scattering are discussed in Appendix B. Other published results are included in the table for comparison. The agreement between the shape of the present elastic DCS and that for the theoretical calculations of Fink and Yates³⁸ is very good.

The DDCS at 2, 4, 10, 20, and 40 eV of ejected energy are presented as a function of the ejection angle in Figs. 18–22 along with the suggested values of Kim¹² and the data by Opal *et al.*⁴ There does not seem to be any published experimental data at this incident energy since the measurements by Opal *et al.* Between 4 and 40 eV ejected energy, the suggested values by Kim are generally lower than the present measurement. At 4 eV the results of Opal *et al.*⁴ are about 25% lower than the present measurement at around 90° and show a totally different angular distribution. Above $W=6$ eV (not shown) the Opal *et al.* results show a similar angular variation as the present data except at 30° where their data are too small. There is better agreement between these two measurements at this primary energy than at 200 or 500 eV. The agreement can be seen to improve with increase in ejected energy. Lastly, the suggested values of Kim are in very good agreement with the Opal *et al.* results above ~ 10

TABLE V. Comparison of the present experimental elastic DCS for 1000-eV electrons with literature values. All values are given in units of 10^{-20} cm²/sr. See the caption of Table II for further details.

θ (deg)	Present expt.	Fink and Yates ^a	Jansen <i>et al.</i> ^b
30	99.3	88.1	87.4
45	22.7	[23.1]	22.0
60	8.45	8.51	
75	3.80	[4.01]	
90	2.20	2.24	
105	1.38	[1.43]	
120	1.02	1.01	
135	0.87	[0.78]	
150	0.68	0.66	

^aReference 38.

^bReference 26.

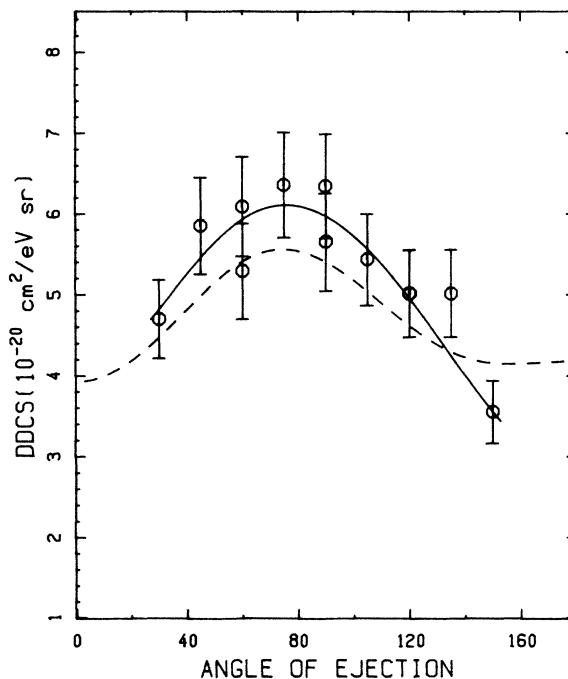


FIG. 18. Absolute DDCS for He for 2 eV ejected energy and 1000 eV primary energy. Circles denote the present experiment. Solid line is a fit to a Legendre-polynomial expansion using the present data. Dashed line is the recommended curve of Kim.

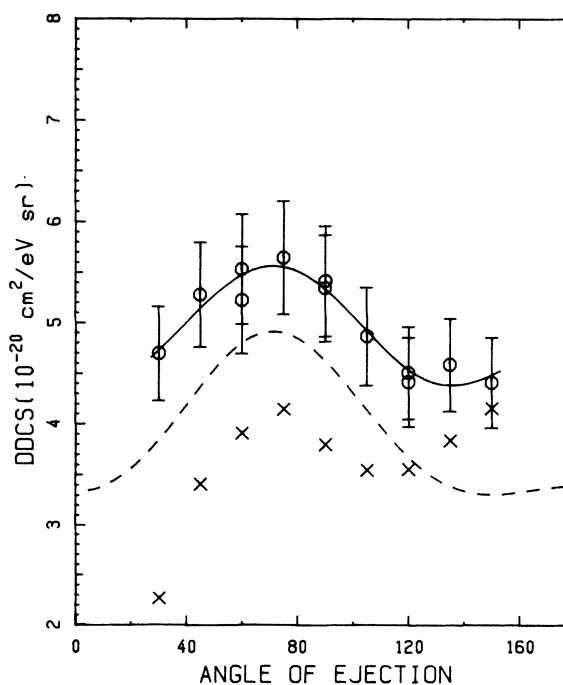


FIG. 19. Absolute DDCS for He for 4 eV ejected energy and 1000 eV primary energy. Crosses denote the data by Opal *et al.* See the caption to Fig. 18 for the definition of other symbols.

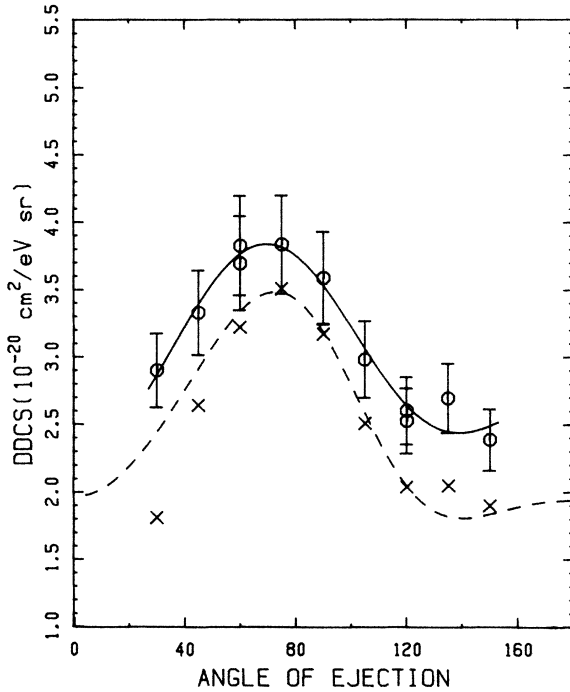


FIG. 20. Absolute DDCS for He for 10 eV ejected energy and 1000 eV primary energy. For the definition of symbols see the captions to Figs. 18 and 19.

eV except at 30° . The 2 eV ejected energy data presented in Fig. 18 need some explanation. The solid curve is a fit to the data excluding the data points at 135° and a repeated measurement at 120° which lie about 50% below the values given by this curve. These data were scaled by this amount and are plotted in the figure as solid circles. The

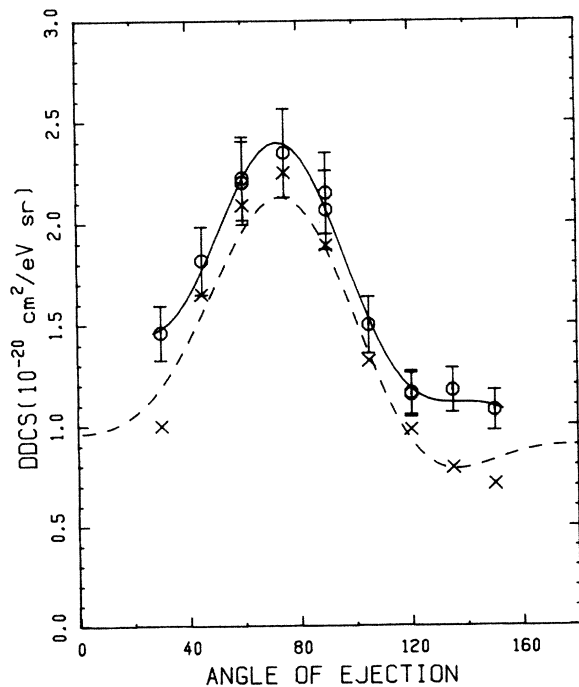


FIG. 21. Absolute DDCS for He for 20 eV ejected energy and 1000 eV primary energy. For the definition of symbols see the captions to Figs. 18 and 19.

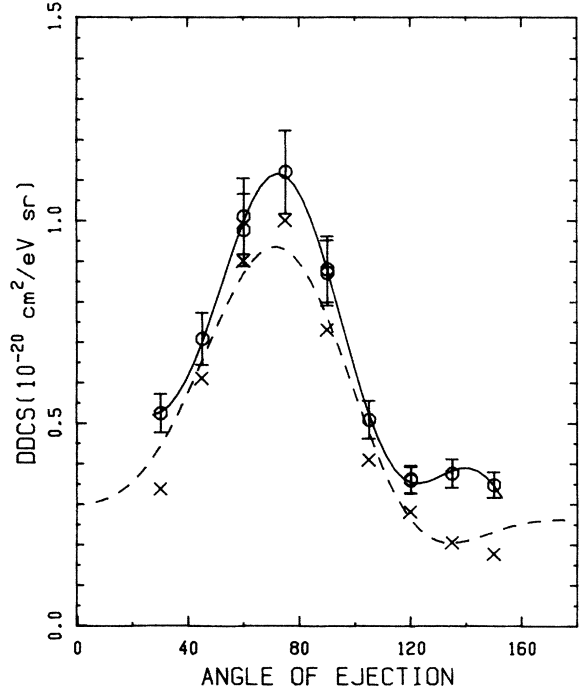


FIG. 22. Absolute DDCS for He for 40 eV ejected energy and 1000 eV primary energy. For the definition of symbols see the captions to Figs. 18 and 19.

reason for doing this is that there was a loss of transmission for these low-energy electrons and, by scaling, all the measurements are brought to a constant transmission at this ejected energy. A comparison of the two spectra at 120° ejection angle is presented in Fig. 23. This shows a gradual increase in the difference between the two spectra from 6 eV down to about 2 eV with no sign of the shape resonance of nitrogen at 2.5 eV, which would have been present if the transmission loss had originated from a high partial background pressure of nitrogen. Hence we

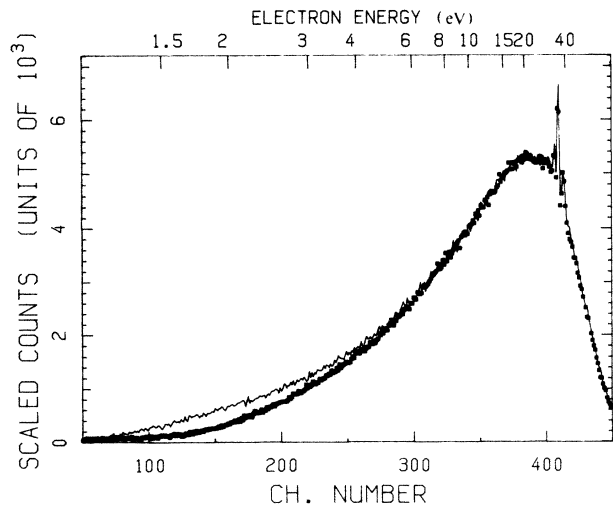


FIG. 23. A comparison plot of two measurements made at 120° scattering angle and 1000 eV primary energy illustrating the loss of transmission for low-energy electrons over time. The two spectra were obtained 10 days apart with the lower transmissions spectrum obtained later.

believe that the smooth loss in transmission below 3.5 eV is an indication of transmission loss as opposed to a change in absorption cross section.

A plot of $Y(E, T)$ for 1000 eV primary energy is shown in Fig. 12. From the procedure stated in Sec. V A, σ_{ion} was computed and is given in Table III. Other reported measurements were also included for comparison. Within the accuracy of the present measurement, there is good agreement among the various values.

D. 2000-eV primary electrons

At this energy, the experiment was carried out in the angular range of 30° to 150° in steps of 15° . The experiment was repeated at 60° and 120° . At this energy, the elastic scattering intensity at $\theta > 90^\circ$ is quite small. The procedure of placing of various spectra on a relative scale as we did earlier *was not done at this energy*. Instead each spectrum was individually normalized at each angle to the elastic DCS calculated by Fink⁴⁰ in the Born approximation. Comparisons could be made between these theoretical results and the values of Jansen *et al.*²⁶ at 30° and 45° . The values used for normalization are presented in Table VI. The corrections for inelastic scattering contribution to the elastic line are given in Appendix B.

The DDCS at 2, 4, 10, 20, and 40 eV are presented in Figs. 24–28. The only other experiment so far reported is by Opal *et al.*⁴ At $W=4$ eV the Opal *et al.* results appear to peak more sharply than the present results and are lower than the present results by 10–30%. Again a difference in the angular distribution between these results is apparent. The deviation is greatest at the extreme angles. The concordance between these two experiments seems to improve with higher ejected energy and at 40 eV ejected energy they are in fair agreement. The suggested values of Kim¹² are about 10% lower than the present results above 60° and for ejected energies above 10 eV. At 4 eV there is good agreement between these two results except at 135° and 150° , where the present results are higher. At 2 eV ejected energy transmission problems were again encountered. The chronological order in which the experiments were carried out was 120° , 90° , 75° , 60° , 45° , 150° , 135° , 105° , 60° , 30° , and 120° . The plotted experimental data clearly indicated a sudden change in the transmission

TABLE VI. Elastic DCS values used for normalization for 2000-eV electrons. All values are in units of 10^{-20} cm²/sr.

θ (deg)	Fink and Yates ^a	Jansen <i>et al.</i> ^b
30	26.4	26.3
45	6.08	6.05
60	2.14	
75	0.985	
90	0.544	
105	0.344	
120	0.243	
135	0.187	
150	0.157	

^aReference 40.

^bReference 26.

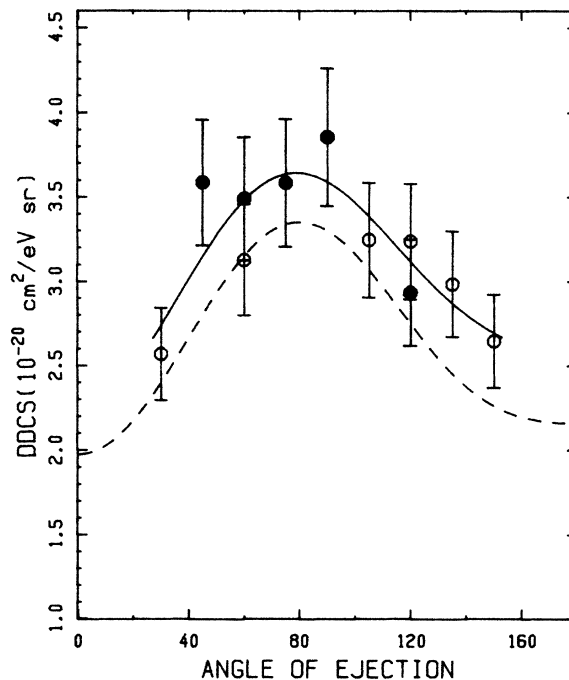


FIG. 24. Absolute DDCS for He for 2 eV ejected electron energy and 2000 eV primary energy. Circles denote the present results. Solid circles represent cross-section measurements corrected for low transmission. Solid line is a fit to a Legendre-polynomial expansion. Dashed line is the recommended curve of Kim.

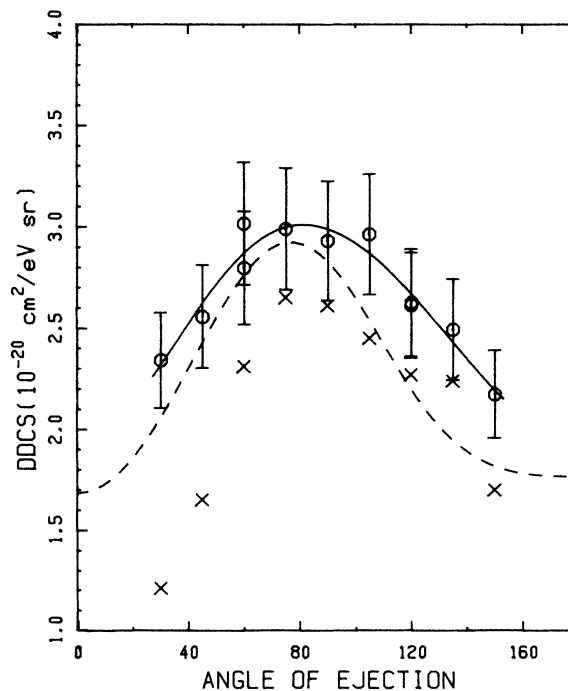


FIG. 25. Absolute DDCS for He for 4 eV ejected electron energy and 2000 eV primary energy. Crosses denote the measurements by Opal *et al.* See the caption to Fig. 24 for the definition of other symbols.

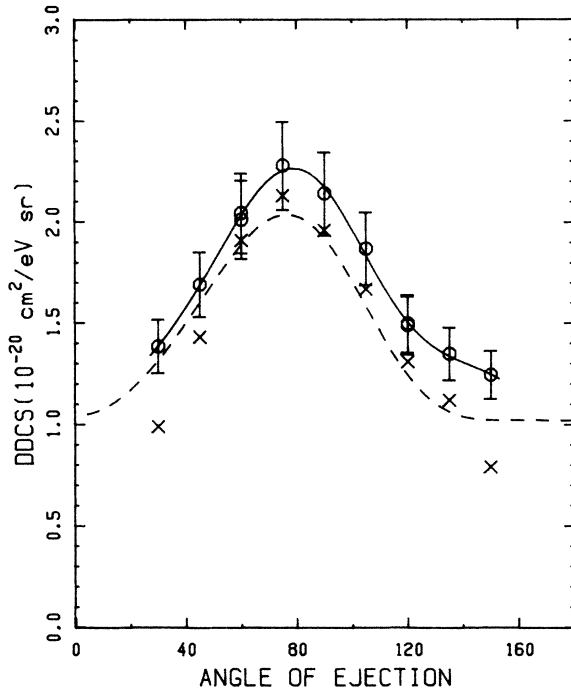


FIG. 26. Absolute DDCS for He for 10 eV ejected energy and 2000 eV primary energy. For the definition of symbols see the captions to Figs. 24 and 25.

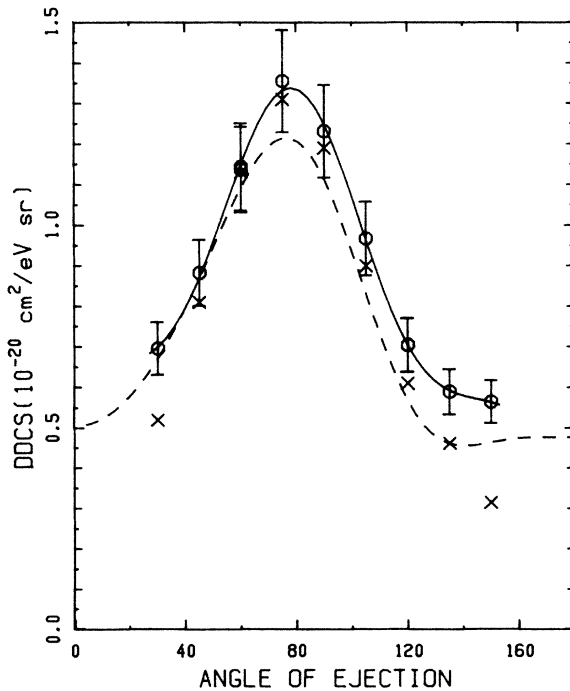


FIG. 27. Absolute DDCS for He for 20 eV ejected energy and 2000 eV primary energy. For the definition of symbols see the captions to Figs. 24 and 25.

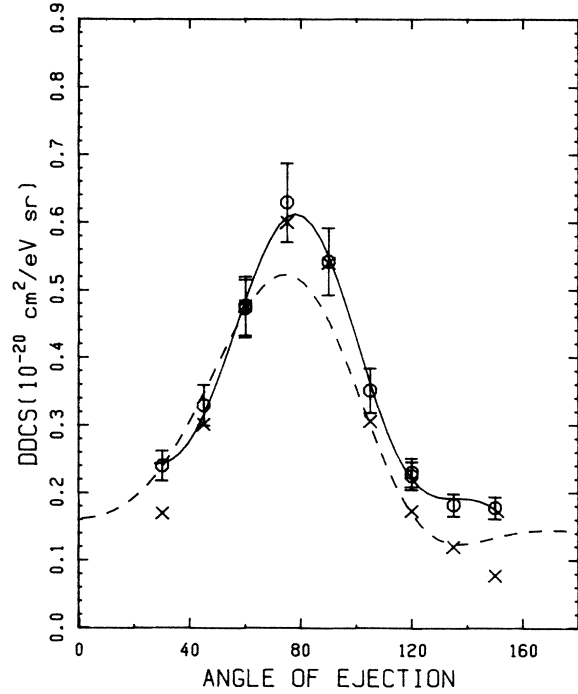


FIG. 28. Absolute DDCS for He for 40 eV ejected energy and 2000 eV primary energy. For the definition of symbols see the captions to Figs. 24 and 25.

for 2-eV electrons in going from 45° to 150°. In other words, the data appear to fall on two different smooth curves. We corrected the data at 120°, 90°, 75°, 60°, and 45° by 40% to bring the data to the higher observed transmission. The corrected data are represented by the solid circles in Fig. 24.

A plot of $Y(E, T)$ is given in Fig. 12 for 2000 eV primary energy and the derived σ_{ion} is presented in Table III along with comparisons.

VI. COMPARISON OF THE PRESENT DDCS DATA WITH BORN CALCULATIONS

In this section we compare the present DDCS data with the theoretical values of Bell and Kingston⁹ who used a Coulomb wave function for the ejected wave and plane waves for the incident scattered electrons. This calculation was carried out in the first Born approximation and only the first five partial waves were used for the ejected electron wave function. For the ground-state wave function for helium, they used the six-parameter Hylleraas wave function of Stewart and Webb.⁴¹ They also ensured the orthogonality between the initial and final states. This calculation appears to be more sophisticated than other calculations reported in the literature.⁴²⁻⁴⁵ Their calculated numbers were quoted to be accurate to $\pm 5\%$ within the Born approximation. This conclusion was reached by comparing the results obtained from calculations based on velocity and length formulations. These authors have given their results in numerical form. In Table VII, the present experimental DDCS are compared with the Born calculations of Bell and Kingston for incident energies of 200, 1000, and 2000 eV. Since they did not present any

TABLE VII. Comparison of the present experimental DDCS at various impact energies (T) with the Born calculations of Bell and Kingston. The DDCS are in units of $10^{-20} \text{ cm}^2 \text{ sr}^{-1}$. The ejected energy is denoted by W . Both W and T are given in eV. The figure in parentheses denotes the power of 10 by which the number is to be multiplied.

W	Ejection angle									
	30°		60°		90°		120°		150°	
	Expt.	Theory	Expt.	Theory	Expt.	Theory	Expt.	Theory	Expt.	Theory
$T=200 \text{ eV}$										
2	1.93(1)	1.99(1)	1.66(1)	1.83(1)	1.40(1)	1.42(1)	1.80	1.32(1)	2.71(1)	1.61(1)
4	1.47(1)	1.85(1)	1.39(1)	1.72(1)	1.19(1)	1.22(1)	1.32(1)	1.01(1)	1.93(1)	1.23(1)
10	8.45	1.40(1)	9.69	1.35(1)	8.14	7.67	7.09	5.15	9.42	6.31
20	4.64	8.83	6.33	8.87	4.27	3.69	2.84	2.06	3.86	2.52
40	2.13	4.60	3.16	4.27	1.45	9.61(-1)	8.64(-1)	5.19(-1)	1.23	6.33(-1)
$T=500 \text{ eV}^a$										
2	7.72	9.81	8.23	1.05(1)	8.18	9.25	8.81	7.46	1.01(1)	7.22
4	7.65	8.58	7.73	9.49	7.21	7.90	7.11	5.75	8.11	5.53
10	4.87	5.74	5.77	6.87	4.98	5.16	3.98	2.96	4.64	2.80
20	2.55	3.17	3.57	4.26	2.83	2.79	1.76	1.17	2.01	1.10
40	9.46(-1)	1.27	1.68	2.09	1.13	9.86(-1)	5.11(-1)	2.68(-1)	6.46(-1)	2.61(-1)
$T=1000 \text{ eV}$										
2	4.82	4.79	5.93	5.83	5.97	5.70	4.96	4.77	3.56	4.42
4	4.73	4.18	5.47	5.23	5.33	4.94	4.54	3.82	4.49	3.52
10	2.86	2.72	3.76	3.70	3.53	3.33	2.64	2.13	2.49	1.94
20	1.48	1.41	2.22	2.20	2.07	1.88	1.18	9.29(-1)	1.10	8.36(-1)
40	5.26(-1)	5.06	1.00	1.00	8.76(-1)	7.66(-1)	3.54(-1)	2.54(-1)	3.46(-1)	2.34(-1)
$T=2000 \text{ eV}$										
2	2.74	2.53	3.48	3.35	2.65	3.49	2.78	2.89	2.69	2.40
4	2.32	2.18	2.87	2.96	2.99	3.01	2.67	2.34	2.19	1.94
10	1.38	1.38	2.03	2.02	2.17	2.02	1.50	1.34	1.25	1.09
20	6.98(-1)	6.89(-1)	1.15	1.14	1.25	1.15	7.02(-1)	6.07(-1)	5.63(-1)	4.77(-1)
40	2.43(-1)	2.32(-1)	4.85(-1)	4.81(-1)	5.49(-1)	4.83(-1)	2.20(-1)	1.74(-1)	1.75(-1)	1.37(-1)

^aThe theoretical values given here are calculated by the present authors using a two-term Clementi and Roetti wave function. See the text for details.

numerical values at $T=500 \text{ eV}$, we calculated the DDCS in the Born approximation using a two-term Hartree-Fock wave function for the helium ground state by Clementi and Roetti.⁴⁶ These results are given in Table VII. A brief outline of the calculation is in order.

The present calculation method involved numerical integrations over the scattering angles of the triple-differential cross section (TDCS). This in turn is calculated analytically as described by Brothers and Bonham.⁴⁷ In this calculation the orthogonality between the initial and final states was ensured. The effective charge on the ion formed in the collision was taken as unity. The Mott cross section in the factorized Born description of ionization was modified to be

$$\left(\frac{d\sigma}{d\Omega} \right)_{\text{Mott}} = \frac{4}{K^4} \left[1 - \frac{2K^2}{k_i^2 + k_s^2} + \left(\frac{2K^2}{k_i^2 + k_s^2} \right)^2 \right], \quad (15)$$

where K is the momentum transfer and k_i and k_s are the momenta of the incident and scattered electrons, respectively. Note that this form is invariant to the exchange of k_i and k_s . Actually, the results were quite insensitive to

the form used for the Mott cross section. Using the Rutherford cross section instead of the Mott cross section did not change the result by more than a few percent. Finally, the use of a two-term wave function for the Hartree-Fock description of the ground state instead of a more accurate five-term one was investigated in Ref. 47 and it was concluded that the two-term function is adequate.

The present calculated results at 2000 eV impact energy are in quite good agreement with those by Bell and Kingston at all but very large angles, where the present calculated DDCS are lower. Even at 200 eV the agreement was quite good between 30° and 120°. Hence, we believe that the present calculated numbers at 500 eV incident energy are of comparable accuracy to those by Bell and Kingston at other incident energies in the angular range of 30° to 120°.

A perusal of Table VII suggests that there is good agreement between the theory and experiment near the broad maximum in the angular distributions of secondary electrons at 1000 and 2000 eV. However, the theoretical values are lower by ~25% than the experimental values

at angles of ejection greater than 90° at these primary energies. At 200 eV, the theoretical values are larger than the experimental values in the forward angles but are smaller in the backward angles. At 500 eV the agreement between the theory and experiment is reasonable.

A comparison of our calculations with those by Bell and Kingston suggests that the electron correlation in the ground-state wave function for helium increases the DDCS in the backward direction. The recoil peak in the TDCS is known¹² to contribute to the DDCS in the backward angles. The disagreement between the theory and experiment seems to suggest that improved description of the recoil peak in TDCS is necessary. It is also important to note that the various approximations in the calculation of the TDCS such as the impulse and binary-encounter approximations affect the recoil peak.⁴⁸ Better theoretical calculations seem to be necessary for accurate values of the DDCS at large ejection angles.

VII. CONCLUSIONS

In this paper we have presented the relative measurements of the double-differential cross sections for 200-, 500-, 1000-, and 2000-eV electrons which are placed on an absolute scale by normalizing the elastic intensity at selected angles to absolute measurements. Also presented are the normalized elastic differential cross sections at 200, 500, and 1000 eV at angles from 30° to 150° .

Photons resulting from the collisions of electrons with helium atoms are found to be isotropically distributed. This result was used to check the relative scale determination in the present experiment.

The present experimental method of determining the double-differential cross sections for secondary electron production is an alternative method to the one using electrostatic analyzers. Because of the single aperture used to define the scattering volume in this experiment, secondary electron production from the slits and apertures normally found in such experiments is greatly reduced. The present data below 4 eV may be inaccurate due to transmission problems but our experimental values in this region should be lower bounds to the actual values.

The DDCS are significantly different from those reported by Opal *et al.*⁴ and are in agreement with those by Erhardt *et al.*⁸ in shape of the angular variation. It is found that the measurements by Erhardt *et al.* at 500 eV primary energy and 40 eV ejected energy are lower by about 40% than the present experiment even though both these measurements agree in shape. It is to be noted that the present experiment was carried out over all ejected and scattered energies at a constant angle. However, Erhardt *et al.* have energy selected a particular ejected electron energy and varied the angle. This means that if the angular distributions of Erhardt *et al.* are correct at a particular ejection energy and if our results are in agreement with theirs in both shape and magnitude then we must be correct at all other energies with the possible exception of energies below 4 eV where transmission problems can arise. This argument suggests that there may be problems in the determination of the absolute scale for the data of Erhardt *et al.* at high ejection energies for 500 eV pri-

mary energy. Lastly, the present experiment does not suggest the peaking of the DDCS at small angles reported by Rudd and DuBois⁶ and Shyn and Sharp.⁷

For convenience in using the data presented in this paper the coefficients of the Legendre-polynomial fit are given in Table VIII for all incident energies and selected ejected electron energies.

The energy distributions of the ejected electrons at all the primary energies clearly show a peak at 35.5 eV as shown in Fig. 12, corresponding to autoionization from the $2s2p$ state with the possibility of an admixture from that due to the $2p^2$ state. Another peak of smaller height can also be seen starting at 39.1 eV corresponding to autoionization from $2s3p$ and higher states. There seems to be a change in slope of the scaled energy distributions of the Platzman plot around the autoionization region. From the Platzman plots the total ionization cross sections were determined and are in good agreement with those by Rapp and Englander-Golden³⁵ and Smith.³⁶

The original experimental data are available from the Physics Auxiliary Publication Service (PAPS).⁴⁹

ACKNOWLEDGMENTS

This work was supported by the National Science Foundation under Grant No. CHE-83-09934.

APPENDIX A: PHOTON YIELD FROM HELIUM EXCITED BY 500-eV ELECTRONS AND RESONANT ABSORPTION BY THE REST GAS

In the electron-impact excitation of helium, for electrons of energy greater than 25 eV, the main inelastic channels available are the excitations to discrete states, corresponding to the $n^1P \leftarrow 1^1S$ transitions. These occur⁵⁰ at energy losses between 21.2 and 24.6 eV. Light emitted in the deexcitation of these levels would be detected along with the elastically scattered electrons. Here we assume that the emitted light, which was not frequency selected, originates mainly from atoms in n^1P states. It was found that the light is isotropically distributed. This is expected to be the case if radiation trapping becomes significant. Other inelastic processes involving excitations to the doubly excited states such as the $2s2p$ state decay predominantly via autoionization⁵¹ rather than by radiative decay. Excitations to triplet states are not very probable at the excitation energies considered here.⁵² In this appendix we present a calculation of the probability for absorption by the rest gas for photons originating from the scattering center. It will be shown here that the radiation trapping is very significant. A pressure variation study on the detected photon yield was carried out and comparisons were made with theoretical model calculations.

The transmission probability calculation is adopted from a method developed by Ladenburgh and Reiche⁵³ in connection with the line absorption in a resonance lamp. An excellent account of this calculation was given by Mitchell and Zemansky⁵⁴ and their notation is employed here.

TABLE VIII. Legendre-polynomial fit coefficients A_n for selected ejected electron energies W and at different primary energies T , in units of $10^{-20} \text{ cm}^2 \text{ sr}^{-1}$. Both W and T are given in eV. See Eq. (10) in the text for details. The number in parentheses denotes the power of 10 by which the number is to be multiplied.

W	A_0	A_1	A_2	A_3	A_4	A_5
$T=200 \text{ eV}$						
2	1.82(1)	-3.55	8.10	-2.44	-3.05(1)	
4	1.41(1)	-1.63	4.56	-2.61	1.56(-1)	
6	1.17(1)	-9.13(-1)	1.68	-3.01	4.05(-2)	
8	9.60	1.21(-1)	9.21(-1)	-2.69	-1.63(-1)	
10	8.49	3.88(-1)	7.14(-1)	-2.53	2.00(-2)	
15.9	5.57	1.10	-6.38(-2)	-2.58	-6.97(-1)	
20	4.39	1.37	-1.98(-1)	-2.44	-5.93(-1)	
40	1.74	1.06	-7.61(-2)	-1.39	-8.92(-1)	8.26(-2)
50	1.09	9.27(-1)	7.36(-5)	-9.48(-1)	-8.61(-1)	-7.97(-2)
$T=500 \text{ eV}$						
2	8.55	-1.15	6.20(-1)	-6.59(-1)	-1.61(-1)	
4	7.50	2.27(-3)	6.03(-1)	-7.08(-1)	3.06(-2)	
6	6.45	3.29(-1)	2.22(-1)	-1.06	6.34(-2)	
8	5.56	5.02(-1)	-1.26(-1)	-1.15	4.36(-2)	
10	4.87	6.29(-1)	-1.88(-1)	-1.33	5.64(-2)	
15.9	3.31	8.29(-1)	-4.53(-1)	-1.34	-7.30(-2)	2.85(-1)
20	2.60	7.83(-1)	-5.06(-1)	-1.13	-8.02(-4)	1.76(-1)
40	1.01	4.93(-1)	-3.56(-1)	-7.19(-1)	-1.46(-1)	2.56(-1)
50	6.47(-1)	4.15(-1)	-1.70(-1)	-5.70(-1)	-1.53(-2)	2.59(-1)
$T=1000 \text{ eV}$						
2	5.21	8.03(-1)	-1.62	-1.93(-1)	-1.28(-1)	
4	4.98	3.79(-1)	-5.95(-1)	-6.40(-1)	1.59(-1)	
6	4.24	4.28(-1)	-6.33(-1)	-6.94(-1)	1.48(-1)	
8	3.64	4.91(-1)	-6.97(-1)	-5.63(-1)	5.69(-2)	
10	3.13	4.87(-1)	-7.38(-1)	-7.24(-1)	8.09(-2)	
15.9	2.14	4.69(-1)	-7.05(-1)	-7.03(-1)	1.75(-1)	
20	1.68	5.09(-1)	-6.35(-1)	-5.39(-1)	1.87(-1)	3.40(-1)
40	6.57(-1)	3.05(-1)	-3.72(-1)	-3.26(-1)	6.43(-2)	3.05(-1)
50	4.16(-1)	2.44(-1)	-2.56(-1)	-2.57(-1)	8.27(-2)	2.58(-1)
$T=2000 \text{ eV}$						
2	3.20	1.29(-1)	-7.77(-1)	-2.72(-1)		
4	2.67	1.11(-1)	-6.66(-1)	-1.05(-1)	-4.78(-2)	
6	2.38	1.81(-1)	-7.32(-1)	-2.85(-1)	2.06(-1)	5.84(-2)
8	2.02	1.82(-1)	-7.20(-1)	-3.30(-1)	1.28(-1)	3.99(-2)
10	1.74	2.29(-1)	-7.21(-1)	-3.18(-1)	1.41(-1)	1.17(-1)
15.9	1.19	2.29(-1)	-5.65(-1)	-2.73(-1)	1.77(-1)	1.15(-1)
20	9.25(-1)	2.05(-1)	-4.93(-1)	-2.50(-1)	1.81(-1)	1.32(-1)
40	3.62(-1)	1.24(-1)	-2.68(-1)	-1.35(-1)	1.13(-1)	1.31(-1)
50	2.29(-1)	9.95(-2)	-1.94(-1)	-1.03(-1)	8.95(-2)	1.25(-1)

The transmission probability T_n is related to the emission line profile E_ω by the relation

$$T_n = \frac{\int_{-\infty}^{\infty} E_\omega \exp(-\sigma_0 n_g L E_\omega) d\omega}{\int_{-\infty}^{\infty} E_\omega d\omega}, \quad (\text{A1})$$

where

$$E_\omega = e^{-\omega^2} - \frac{2a}{\sqrt{\pi}} [1 - 2\omega F(\omega)]. \quad (\text{A2})$$

In Eq. (A1), σ_0 is the maximum absorption coefficient for a chosen emission line in He, n_g is the average number

density ($5.15 \times 10^{12} \text{ cm}^{-3}$ at a background pressure of 160 μTorr), and L is the path length for the photon (43.5 cm). In Eq. (A2), $F(\omega)$ is the Dawson integral⁵⁵ and a is proportional to the ratio of the natural ($\Delta\nu_N$) to the Doppler ($\Delta\nu_D$) width of the absorption line as

$$a = \sqrt{\ln 2} \frac{\Delta\nu_N}{\Delta\nu_D}. \quad (\text{A3})$$

Using the above equations and parameters shown in Table IX T_n was calculated for the emission lines, $n^1P \rightarrow 1^1S$ for $n=2, 3, 4$, and 5. The probability for pro-

TABLE IX. Parameters used in the calculation of the yield parameter Y_{ph} .

State	f^a	τ^b (ns)	Δv_N^c (10^7 s^{-1})	Δv_D^d (10^{10} s^{-1})	a	σ_0^e (\AA^2)	σ_{ex}^f (\AA^2)
2^1P	0.276 15	0.58	27.4	3.19	0.007 15	2160	0.06 84
3^1P	0.073 47	1.84	8.65	3.47	0.002 08	575	0.01 69
4^1P	0.030 19	4.23	3.76	3.57	0.000 877	236	0.00 679
5^1P	0.015 21	8.19	1.94	3.62	0.000 446	119	0.00 340

^aThese values are taken from Ref. 1, p. 77.

^bCalculated using the relation, $\tau = (3mc/8\pi^2e^2)(\lambda_0^2/f)$.

^cCalculated from the relation $\Delta v_N = 1/2\pi\tau$.

^dCalculated using the relation $\Delta v_D = 7.16 \times 10^{-7} v_0 (T/M)^{1/2}$.

^eCalculated using the relation $\sigma_0 = (2/\Delta v_D)(\ln 2/\pi)^{1/2}(\pi e^2/mc)f$.

^fTaken from Table 3.24 of Ref. 6.

ducing atoms in different excited states by electron impact is proportional to the total excitation cross sections. These were calculated by Bransden and McDowell⁵⁶ in the first Born approximation for 500-eV electrons and were employed in the present calculation. An effective photon yield parameter Y_{ph} , which is a function of the background pressure P , can be defined as

$$Y_{ph}(P) = \sum_{n=2}^5 \sigma_{ex}(1^1S \rightarrow n^1P) T_n(n^1P \rightarrow 1^1S), \quad (\text{A4})$$

where $\sigma_{ex}(1^1S \rightarrow n^1P)$ is the total cross section for the excitation $1^1S \rightarrow n^1P$ and $T_n(n^1P \rightarrow 1^1S)$ is the transmission probability corresponding to the emission line $n^1P \rightarrow 1^1S$. The $Y_{ph}(P)$ for background pressures of 80 to 160 μTorr were calculated and are given in Table X.

The number of photons detected per second, N_{ph} , when an electron beam of current i_0 interacts with a gas beam of density n_0 along a distance l , can be written as

$$N_{ph}(P) = i_0 n_0 l \left[\frac{\Delta\Omega}{4\pi} \right] \eta_{ph} Y_{ph}(P), \quad (\text{A5})$$

where η_{ph} is the detector sensitivity to photons and $\Delta\Omega$ is the solid angle of detection. Here we assumed that η_{ph} does not change with the photon energy in the range 21.22

TABLE X. Variation of effective photon yield $Y_{ph}(P)$ with the background pressure P . $Y_{ph}(P)$ is given in units of 10^{-18} cm^2 .

P (μTorr)	$Y_{ph}(P)$
80	0.494
88	0.445
96	0.404
104	0.370
112	0.340
120	0.314
128	0.291
136	0.271
144	0.254
152	0.238
160	0.224

to 24.04 eV. A similar expression for the number of elastically scattered electrons per second, N_{el} , in a direction θ , from the electron beam direction is written as,

$$N_{el} = i_0 n_0 l \frac{d\sigma}{d\Omega}(\theta) \Delta\Omega \eta_{el} \quad (\text{A6})$$

where $d\sigma(\theta)/d\Omega$ is the elastic DCS and η_{el} is the detector efficiency for elastically scattered electrons. Note that the absorption of these electrons by the rest gas is a negligible effect (1%). A ratio $R(P)$, of Eq. (A5) to Eq. (A6), is defined as

$$R(P) = \frac{N_{ph}}{N_{el}} = \frac{\eta_{ph}}{\eta_{el}} \left[\frac{1}{4\pi} \right] \frac{Y_{ph}(P)}{(d\sigma/d\Omega)}. \quad (\text{A7})$$

An experimental value of 0.0795 was observed with 500-eV primary electrons at a scattering angle of 120° when the background pressure was 160 μTorr . Using the calculated $Y_{ph}(P)$ and an elastic DCS (Ref. 38) of $4.32 \times 10^{-20} \text{ cm}^2 \text{ sr}^{-1}$, $R(P)$ is calculated to be 0.4126 assuming that η_{ph} and η_{el} have the same value. However, the disagreement between the model and the experimental value suggests that η_{ph} is less than η_{el} . To eliminate the uncertainty in the calculated $R(P)$ due to the detector sensitivities, we devised a pressure variation study.

The scattering experiment was carried out again at 120° with half the background pressure. The ratio $R(P/2)$ was determined to be 0.1213, which is to be compared with the calculated value of 0.910 under these conditions. The ratio $R(P)/R(P/2)$, given by the relation

$$\frac{R(P)}{R(P/2)} = \frac{Y_{ph}(P)}{Y_{ph}(P/2)}, \quad (\text{A8})$$

is independent of the detector sensitivities. An experimental value for this ratio of 0.655 was observed, while the calculated $Y_{ph}(P)/Y_{ph}(P/2)$ was 0.453 in close agreement with the experiment.

Using the calculated $Y_{ph}(P)$ and experimental $R(P)$ values, the ratio η_{ph}/η_{el} was determined to be 0.19 and a value of 0.13 was obtained using $Y_{ph}(P/2)$ and $R(P/2)$. Assuming that η_{el} is close to 1, this ratio is in agreement with reported photon detection efficiencies⁵⁷ for micro-channel plates.

If the Y values in Table X are divided by the sum of to-

tal electron excitation cross section σ_{ex} from Table IX (9.5×10^{-18} cm²), then the fraction of photons emitted from the scattering region which reach the detector without absorption is found to range from 5% to 2% with background pressure varying from 80 to 160 μ Torr. This means that 95–97% of photons reaching the detector were produced by reemission of absorbed radiation by the background gas. Hence we may conclude that the angular dependence of the integrated photon intensity must be highly isotropic. Lastly, we wish to point out that the variation of the effective photon yield function $Y_{ph}(P)$ with the background pressure does not follow a Beer's-law formula. In the pressure range of 80–160 μ Torr a plot of $\ln Y_{ph}(P)$ against the pressure is concave upwards.

APPENDIX B: INELASTIC SCATTERING CONTRIBUTION TO THE ELASTIC LINE INTENSITY

In the present experiment, the energy resolution for scattered electrons at energies of 200, 500, 1000, and 2000 eV is 20, 85, 250, and 700 eV, respectively. At scattering angles greater than 45° the inelastic scattering decreases quite rapidly. Hence one would not expect significant inelastic contributions to the observed intensity of the "elastic" peak. However, at smaller angles and for scattering from helium where the inelastic intensity exceeds the elastic intensity, it is necessary to correct the elastic peak for the inelastic contribution.

The scattered intensity at a given scattering angle θ is taken as

$$I(E_S, E_0, \theta) = \left[\frac{d\sigma}{d\Omega} \right]_{el} \delta(E - E_0) + \frac{d^2\sigma}{dW d\Omega}(E_{SI}, \theta) e^{\lambda_I(E_S - E_{SI})}$$

for $E_S \leq E_{SI}$ (B1)

where E_0 is the primary energy, E_S is the energy of the scattered electron, and $E_{SI} = E_0 - E_{IP}$ with E_{IP} the ioni-

$$I_{inel}(t_1) = \int_0^{t_1} dt I_{inel} = E_{SI} t_{SI}^2 \frac{d^2\sigma}{dW d\Omega} e^{-\lambda_I E_{SI}} \int_{t_{SI}}^{\infty} dt \left[\operatorname{erf} \left[\frac{t_1 - t}{\sqrt{2}\sigma} \right] + \operatorname{erf} \left[\frac{t_0}{\sqrt{2}\sigma} \right] \right] \frac{1}{t^3} \exp(\lambda_I E_{SI} t_{SI}^2 / t^2), \quad (B3)$$

TABLE XII. The percentage ratio of the estimated inelastic contribution to the elastic line intensity. E_0 denotes the primary energy in eV and θ denotes the scattering angle in degrees. At angles above 90° this correction is less than 4%.

E_0	θ				
	30°	45°	60°	75°	90°
200	3	3	3	3	3
500	26	6	6	6	5
1000	29	13	7	6	5
2000	52	11	6	6	4

TABLE XI. Comparison of observed elastic cross sections with the values derived from the elastic peak in the time spectrum after correcting for the inelastic contribution by the proposed scheme. E_0 denotes the primary energy and θ denotes the scattering angle in degrees. The cross sections are in units of 10^{-20} cm²/sr.

E_0	θ	$(d\sigma/d\Omega)_{el}^a$	$(d\sigma/d\Omega)_{el}$
		observed	derived
200	30	905	920
	50	287	290
	90	65.0	65.9
	150	23.5	23.9
400	30	394	375
	50	93	91
	90	18.4	18.1
	150	5.09	5.00

^aCrooks, Ref. 28.

zation potential of helium (24.6 eV), $(d\sigma/d\Omega)_{el}$ is the elastic scattering cross section, $d^2\sigma/dW d\Omega$ is the DDCS, and λ_I is an adjustable parameter. With appropriate choice of λ_I the modeled DDCS [second term on the right-hand side of Eq. (B1)] was found to give an adequate representation of the data presented by Crooks.²⁸ Equation (B1) is converted into a time-of-flight spectrum and then folded with a Gaussian-shaped time broadening function. The elastic intensity integrated from time zero to a limit t_1 is found to be

$$I_{el}(t_1) = \int_0^{t_1} dt I_{el} = \frac{1}{2} \left[\frac{d\sigma}{d\Omega} \right]_{el} \left[\operatorname{erf} \left[\frac{t_1 - t_0}{\sqrt{2}\sigma} \right] + \operatorname{erf} \left[\frac{t_0}{\sqrt{2}\sigma} \right] \right], \quad (B2)$$

where erf stands for the error function and σ is the rms half-width of the time broadening function. The inelastic intensity integrated from time zero to a limit t_1 is found to be

where $t_{SI} = (ml^2/2E_{SI})^{1/2}$. Here m is the mass of the electron and l is the flight distance.

From Eqs. (B2) and (B3), we calculated the expected time spectrum and the spectrum transformed to $d^2\sigma/dW d\Omega$ using the data of Crooks for incident energies of 200 and 400 eV and angles of 30°, 50°, 90°, and 150° in each case. The area under the elastic line in the time spectrum was integrated over a time width corresponding to five channel widths of the MCA bracketing its maximum. A correction for inelastic pollution was defined as the product of the observed cross section at the low-energy boundary of the peak (E_{\min}), and the energy width of the inelastic contribution in this region,

$E_0 - E_{\min} - E_{IP}$. This estimate of the inelastic contribution was then subtracted from the integrated elastic peak area of the time spectrum. The elastic cross sections derived in this manner are compared to the original values of Crooks in Table XI. The agreement suggests that the proposed scheme for correcting for the inelastic contribution is valid.

This estimation procedure is employed for primary energies of 200, 500, 1000, and 2000 eV at all scattering angles. In Table XII the ratios of the estimated inelastic contribution to the elastic line to the elastic intensity are presented.

- ¹M. Inokuti, in Radiological and Environmental Research Division Annual Report, October 1976–September 1977, Argonne National Laboratory Report No. ANL-77-65, 1977 (unpublished); Y. Hatano, in Argonne National Laboratory Report No. ANL-84-28, 1984 (unpublished). A good exposition of the various uses for these cross sections are given in the first nine articles in this report.
- ²C. B. O. Mohr and F. H. Nicoll, Proc. R. Soc. London Ser. A **144**, 596 (1934).
- ³M. Goodrich, Phys. Rev. **52**, 259 (1937).
- ⁴C. B. Opal, E. C. Beaty, and W. K. Peterson, At. Data **4**, 209 (1972).
- ⁵N. Oda, F. Nishimura, and S. Tahira, J. Phys. Soc. Jpn. **33**, 462 (1972).
- ⁶M. E. Rudd and R. D. DuBois, Phys. Rev. A **16**, 26 (1977).
- ⁷T. W. Shyn and W. E. Sharp, Phys. Rev. A **19**, 557 (1979).
- ⁸H. Erhardt, K. Jung, R. Muller-Fiedler, and P. Schlemmer, Argonne National Laboratory Report No. ANL-84-28, 1983 (unpublished).
- ⁹K. L. Bell and A. E. Kingston, J. Phys. B **8**, 2666 (1975).
- ¹⁰S. Tahira and N. Oda, J. Phys. Soc. Jpn. **35**, 582 (1973).
- ¹¹Y. K. Kim, Radiat. Res. **61**, 21 (1975); **64**, 96 (1975); **64**, 205 (1975).
- ¹²Y. K. Kim, Phys. Rev. A **28**, 656 (1983).
- ¹³Model numbers CE 3K/5U and CE 406 were purchased from Cliftronic, Inc., Clifton, New Jersey.
- ¹⁴R. R. Goruganthu, W. G. Wilson, and R. A. Bonham, Argonne National Laboratory Report No. ANL-84-28, 1983 (unpublished).
- ¹⁵R. R. Goruganthu and W. G. Wilson, Rev. Sci. Instrum. **55**, 2030 (1984).
- ¹⁶R. E. Kennerly and R. A. Bonham, Phys. Rev. A **17**, 1844 (1978).
- ¹⁷H. J. Blaauw, R. J. Wagenaar, D. H. Barends, and F. J. de Heer, J. Phys. B **13**, 359 (1980).
- ¹⁸R. T. Brinkmann and S. Trajmar, J. Phys. E **14**, 245 (1981).
- ¹⁹R. K. Jones and R. A. Bonham, Aust. J. Phys. **35**, 559 (1982).
- ²⁰R. K. Jones, Phys. Rev. A **31**, 2898 (1985).
- ²¹P. G. Coleman, T. C. Griffith, and G. R. Heyland, Appl. Phys. **5**, 223 (1974).
- ²²The solid angle subtended by the interior surface of a ring at any point on the axis can be derived from first principles. However, no closed-form expression for the solid angle subtended at points off the axis may be obtained.
- ²³H. Bruining, *Physics and Applications of Secondary Electron Emission* (Pergamon, London, 1954).
- ²⁴J. L. H. Jonker, Philips Res. Rep. **6**, 372 (1951); see also H. Bruining, Ref. 23, pp. 97 and 98.
- ²⁵R. E. Kennerly, Rev. Sci. Instrum. **48**, 1682 (1976).
- ²⁶R. H. J. Jansen, F. J. de Heer, H. J. Luyken, B. Luyken, B. van Wingerden, and H. J. Blaauw, J. Phys. B **9**, 185 (1976).
- ²⁷J. P. Bromberg, J. Chem. Phys. **61**, 963 (1974); some of the numbers were cited by Byron and Joachain in Ref. 29 as private communication.
- ²⁸G. B. Crooks and M. E. Rudd, Bull. Am. Phys. Soc. **17**, 131 (1971); G. B. Crooks, Ph.D. thesis, University of Nebraska, 1972.
- ²⁹F. W. Byron and C. J. Joachain, Phys. Rev. A **15**, 128 (1977).
- ³⁰S. K. Sethuraman, J. A. Rees, and J. R. Gibson, J. Phys. B **7**, 1741 (1974).
- ³¹Cf. *Handbook of Mathematical Functions with Formulas, Graphs and Mathematical Tables*, edited by M. Abramowitz and I. A. Stegun (Dover, New York, 1972).
- ³²H. S. W. Massey and C. B. O. Mohr, Proc. R. Soc. London Ser. A **140**, 625 (1933); C. B. O. Mohr and F. H. Nicoll, Ref. 2; W. K. Peterson, E. C. Beaty, and C. B. Opal, Phys. Rev. A **5**, 712 (1972).
- ³³T. W. Shyn, Phys. Rev. A **27**, 2388 (1983).
- ³⁴N. Oda and F. Nishimura, in *Abstracts of the Tenth International Conference on the Physics of Electronic and Atomic Collisions, Paris, 1977*, edited by M. Barat and J. Reinhardt (Commissariat à l'Énergie Atomique, Paris, 1977), p. 362.
- ³⁵D. Rapp and P. Englander-Golden, J. Chem. Phys. **43**, 1464 (1965).
- ³⁶P. T. Smith, Phys. Rev. **36**, 1293 (1930).
- ³⁷J. P. Bromberg, J. Chem. Phys. **3**, 1243 (1970).
- ³⁸M. Fink and A. C. Yates, At. Data **1**, 385 (1970).
- ³⁹N. Oda, Radiat. Res. **64**, 80 (1975).
- ⁴⁰M. Fink (private communication). Values were kindly furnished by Fink using the same program and electrostatic potential for helium as used in the published results of Ref. 38.
- ⁴¹A. L. Stewart and T. G. Webb, Proc. Phys. Soc. London **82**, 532 (1963).
- ⁴²N. F. Mott and H. S. W. Massey, *The Theory of Atomic Collisions*, 3rd ed. (Clarendon, Oxford, 1969), p. 184.
- ⁴³S. Tahira and N. Oda, J. Phys. Soc. Jpn. **35**, 582 (1973).
- ⁴⁴S. T. Manson, L. H. Toburen, D. H. Madison, and N. Stolterfoht, Phys. Rev. A **12**, 60 (1975). These authors have used Hartree-Slater one-electron orbitals to construct the ground state, otherwise, the calculation is very similar to that in Ref. 9.
- ⁴⁵T. Burnett, S. P. Rountree, G. Doolen, and W. D. Robb, Phys. Rev. A **13**, 626 (1976). These authors have used a four-state CI wave function for the ground state.

- ⁴⁶E. Clementi and C. Roetti, *At. Data Nucl. Data Tables* **14**, 177 (1974).
- ⁴⁷M. J. Brothers and R. A. Bonham, *J. Phys. B* **17**, 4235 (1984).
- ⁴⁸A. Lahmam-Bennani, H. F. Wellenstein, C. Dal Cappello, M. Raoult, and A. Duguet, *J. Phys. B* **16**, 2219 (1983).
- ⁴⁹See AIP document No. PAPS-PLRAA-34-103-50 for 50 pages of the original experimental data. Order by PAPS number and journal reference from American Institute of Physics, Physics Auxiliary Publication Service, 335 East 45th Street, New York, NY 10007. The price is \$1.50 for each microfiche (98 pages) or \$5.00 for photocopies of up to 30 pages, and \$0.15 for each additional page over 30 pages. Airmail additional. Make checks payable to the American Institute of Physics.
- ⁵⁰J. Berkowitz, *Photoabsorption, Photoionization, and Photoelectron Spectroscopy* (Academic, New York, 1979), p. 77.
- ⁵¹K. Siegbahn, C. Nordling, G. Johansson, J. Hedman, P. F. Hede'n, K. Hamrin, U. Gelius, T. Bergmark, L. O. Werme, R. Manne, and Y. Baer, *ESCA Applied to Free Molecules* (North-Holland, Amsterdam, 1969), p. 30.
- ⁵²R. M. St. John, F. L. Miller, and C. C. Lin, *Phys. Rev.* **134**, A888 (1964).
- ⁵³R. Ladenburgh and F. Reiche, *Ann. Phys. (Leipzig)* **42**, 181 (1913).
- ⁵⁴A. C. G. Mitchell and M. W. Zemansky, *Resonance Radiation and Excited Atoms* (Cambridge University, Cambridge, 1971).
- ⁵⁵The Dawson integral is calculated using the IMSL subroutine, MMDAS, available on the Control Data Corporation Cyber 170/855 computer at Indiana University, Bloomington, Indiana.
- ⁵⁶B. H. Bransden and M. R. C. McDowell, *Phys. Rep.* **46**, 251 (1978).
- ⁵⁷D. de Bruijn *et al.*, in *Technische Informatie Post*, edited by H. Kersten (FOM-Instituut voor Atoom-en Molecuulfysica, Kruislaan Amsterdam) (unpublished).